nature portfolio

Peer Review File

Facile cascade-anchored synthesis of ultrahigh metal loading single-atom for significantly improved Fenton-like catalysis

Corresponding Author: Professor Minghua Zhou

This file contains all reviewer reports in order by version, followed by all author rebuttals in order by version.

Attachments originally included by the reviewers as part of their assessment can be found at the end of this file.

Version 0:

Reviewer comments:

Reviewer #1

(Remarks to the Author)
In this work, the authors constructed different ultrahigh metal loading single atom catalysts by using a facile one-step calcination. Systematic investigation confirms that the powerful ligand-chelation between oxalic acid and metal ions, as well as the simultaneously generated entangled polymer networks are crucial for achieving high-loading SACs. The results in this manuscript are interesting, but these are some issues in structure and DFT calculations. Thus, I would like to recommend the acceptance of this manuscript for the publication in Nature Communication after addressing the following issues.
1. The synthesis of ultrahigh metal loading single atom catalysts has not been extensively explored in this work. There is a lack of detailed describe in experimental section, which are very difficult to repeat for readers.
I) What is the sequence of adding MA, OA, and Fe(NO3)3·9H2O to deionized water? Will different addition sequences affect the final synthesis of the catalyst?
II) What is the intensity of stirring for the mixed solution, and is it stirred at room temperature?
III) How are the products collected? Is centrifugation involved, and is washing required with H2O or other solvents?
IV) Is it necessary for the precursor to undergo thorough grinding before calcination?
V) What are the respective amounts of Fe(NO3)3·9H2O added during the synthesis process of single-atom Fe with different metal loading?
VI) Why are other chelating ligands used in the synthesis process of single-atom Ag and La? What are the criteria for selecting chelating ligands in different single-atom synthesis processes?
2. The results of FTIR suggest that the chelation of Fe3+ with OA did not change the skeleton structure, while the results of XRD and Raman demonstrate that the high-loading Fe atoms significantly altered the skeletal structure of the CN substrate. Please provide the more detailed explain.
3. In Supplementary Fig. 4, the Fe 2p spectra seemingly not shifted towards lower binding energies with increasing Fe loading.
4. As you mentioned, in the process of preparing high-density Fe single atoms, O plays a more crucial role than N, where N functions in coordinating with Fe. What role does O play in this process? Why does O fail to play a similar role in traditional methods of preparing Fe single atoms? The role of O in Fe single atom structure should also be reflected in DFT calculations.
5. In the DFT calculation process, are the structure models of Fe single atoms with different densities used the same as those presented in Supplementary Figs. 7-10? How are such large models computed using VASP? The raw data (include the initial structure files) from the calculation process should be provided to enable readers to replicate the work.
6. In supplementary Fig. 11, is the dashed line representing the position of the Fermi level? Unless specifically stated, the Fermi level in a DOS plot is generally aligned to the zero position. And the PDOS diagrams in supplementary Fig. 11 do not clearly demonstrate the overlap of the 3d orbitals of Fe atoms and the 2p orbitals of N/C atoms increases sequentially with increasing Fe loading. The contribution of Fe 3d orbitals to the pDOS near the Fermi level also do not obvious increases.
7. Due to the strong correlation of d electrons in Fe, the DFT+U is necessary.
8. The structural characterization and DFT calculations of ultra-high-density single-atom catalysts in this paper need to be refined.

Reviewer #2

(Remarks to the Author)
The authors present the preparation of highest metal loading to date on carbon nitride, including transition metals (Fe, Mn), rare earth metal (La), and noble metal (Ag) SAC. The mechanism for such high metal loading was systematically studied, and studied the structure-catalysis conformational relationship by the activation of peroxymonosulfate (PMS) for toxic organics degradation. Therefore, I would recommend it to be published after a major revision by addressing the following comments/questions.

1. In this work, why was carbon nitride chosen as the metal-supporting substrate instead of other high surface area materials (such as graphene, diatomaceous earth, etc.)? What are its advantages?

2. The acid-base properties significantly affect the catalytic performance of Fenton-like catalysts. The paper only demonstrates that Fe-SAC-41.31/PMS system has strong environmental anti-interference ability for SMX degradation under different acidic environments. Therefore, what is the activity of the catalyst in different alkaline environments?

3. In this study, the highest metal load in Fe based SAC to date (41.31 wt%) was obtained through a cascading anchoring strategy, and it demonstrated the best catalytic performance. So, what is the loading limit of Fe? Will more loads lead to better catalytic performance?

4. In Figure 1a and Figure 1b, the image ruler is not high-definition. Please correct it.

Reviewer #3

(Remarks to the Author)
The manuscript presents a strategy for synthesizing high-loading single-atom catalysts (SACs) and their application in activating peroxymonosulfate (PMS) for the degradation of organic pollutants. While the work demonstrates potential application value, several critical issues must be addressed before it can be considered for publication. Below are the detailed concerns that warrant rejection of the manuscript:
1. The proposed cascade anchoring method for synthesizing high-loading SACs lacks sufficient novelty. Similar approaches have been extensively reported in the literature (e.g., Adv. Mater. 2024, 36, 2404900; Nat. Chem. 2021, 13(9): 887-894; Nat. Commun. 2019, 10(1), 1278). Notably, the study in Nat. Commun. 2019 employed glucose as an anchor and C_3N_4 as the substrate, yet achieved significantly lower metal loading compared to the 41.31 wt% reported in this manuscript. The authors fail to provide a convincing explanation for the exceptionally high loading achieved in their work, nor do they elucidate the underlying mechanisms ensuring the stability of these high-loading SACs. Without a clear differentiation from existing methods and a robust mechanistic explanation, the novelty and scientific contribution of the synthesis strategy remain questionable.
2. The manuscript suggests that oxalate plays a critical role in forming a supramolecular network with metal ions and melamine during the precursor stage, thereby enhancing SAC loading. However, the authors do not quantitatively investigate the relationship between the amount of oxalate added and the final SAC loading. Furthermore, there is no in-depth discussion on how oxalate contributes to the high metal loading or how its addition influences the synthesis process. This lack of quantitative analysis and mechanistic insight is a significant drawback, particularly for scaling up the synthesis process, as it leaves key parameters undefined.
3. The decomposition of oxalate during calcination produces CO_2, which may disturb the condensation of melamine and affect the morphology, defects, and porosity of the C_3N_4 support. However, the authors do not systematically investigate whether varying the amount of oxalate can control the porosity and specific surface area of C_3N_4. Additionally, it remains unclear whether the micro- or mesopores generated by CO_2 release positively influence single-atom anchoring efficiency, reactant diffusion, or electron transfer. Excessive oxalate could also compromise the structural integrity of the C_3N_4 framework, potentially reducing catalyst stability or activity.
4. Figure 2d reveals a non-linear, exponential relationship between the initial Fe^{3+} amount and the final iron content in the catalyst. The authors do not provide a satisfactory explanation for this phenomenon. For instance, they do not explore whether there is a concentration-dependent coordination effect between oxalate and Fe^{3+} ions. A mechanistic explanation and experimental comparison are necessary to clarify why higher Fe salt concentrations lead to such an unusual increase in SAC loading. Without this, the synthesis process remains poorly understood.
5. The manuscript lacks a thorough discussion on the coordination environment of single iron atoms at different loadings. Although Figure 2k shows no Fe-Fe coordination peak in the second coordination shell, suggesting the absence of short-range metal-metal bonding, at such high iron loadings (e.g., 41 wt%), there may be more distant or indirect Fe-Fe interactions. These interactions could slightly alter the bond length or coordination environment of the single Fe atoms, potentially influencing catalytic performance.
6. From a kinetic perspective, the apparent rate constant k should theoretically exhibit a linear or quasi-linear relationship with the total number of active sites, assuming each site has similar intrinsic activity. However, the authors do not thoroughly discuss the specific relationship between k and the number of active sites in Figures 3a and S16. If the relationship is nonlinear, and catalytic kinetics accelerate significantly at high loadings, this could suggest the presence of long-distance Fe-Fe interactions that enhance catalytic activity. This point requires further analysis to clarify the underlying mechanisms driving the observed kinetics.
7. The authors propose that high iron loading not only provides more active centers but also thermodynamically facilitates PMS activation, leading to superior pollutant degradation performance. They hypothesize that this is related to Fe-Fe remote interactions. However, the manuscript does not investigate whether there is a critical loading at which these remote interactions become significantly enhanced, thereby playing a crucial role in lowering energy barriers or improving electron

transfer efficiency. This is a key aspect that requires further experimental validation to support the proposed hypothesis.
8. Figures 2g-i demonstrate that other metals (Mn, Ag, La) can also be dispersed at high loadings. However, the authors do not discuss whether the choice of metal salt (e.g., chlorides) affects the cascade anchoring process. This omission limits the understanding of the method's generalizability and applicability to other metal systems. A more comprehensive discussion on the influence of different metal precursors is necessary to establish the broader utility of the proposed synthesis strategy.
9. The manuscript does not provide a detailed discussion on the relationship between sintering temperature and the structure of SACs. Sintering temperature is a critical parameter that can significantly influence the stability, dispersion, and activity of single-atom sites. A more in-depth exploration of this aspect is essential to optimize the synthesis process and ensure the reproducibility of the high-loading SACs.
In conclusion, while the manuscript presents an approach to synthesizing high-loading SACs, the lack of sufficient novelty, insufficient mechanistic insights, and unresolved critical issues lower its scientific rigor and potential impact. Addressing these concerns through additional experiments and a more thorough discussion would be necessary to strengthen the manuscript's contribution to the field. Until then, I recommend rejection of this work.

Reviewer #4

(Remarks to the Author)
I co-reviewed this manuscript with one of the reviewers who provided the listed reports. This is part of the Nature Communications initiative to facilitate training in peer review and to provide appropriate recognition for Early Career Researchers who co-review manuscripts.

Version 1:

Reviewer comments:

Reviewer #1

(Remarks to the Author)
The authors have thoroughly addressed all of my concerns. They have provided detailed responses and made corresponding revisions to the manuscript. I am pleased to recommend the publication of this manuscript in Nature communications.

Reviewer #2

(Remarks to the Author)
I think this paper is acceptable now.

Reviewer #3

(Remarks to the Author)
“The authors have thoroughly and satisfactorily addressed all the questions raised in the previous round of review. The manuscript has been significantly improved. I have no further comments and recommend this manuscript for publication in Nature Communications.”

Reviewer #4

(Remarks to the Author)
I co-reviewed this manuscript with one of the reviewers who provided the listed reports. This is part of the Nature Communications initiative to facilitate training in peer review and to provide appropriate recognition for Early Career Researchers who co-review manuscripts.

Facile cascade-anchored synthesis of ultrahigh metal loading single-atom for significantly improved Fenton-like catalysis

Shuaishuai Li, Wei Wang ⁎, Huizhong Wu, Xuechun Wang, shihu Ding, Jingyang Liu, Xiuwu Zhang, Jiangli Sun, Chunhong Fu, Minghua Zhou *

MOE Key Laboratory of Pollution Processes and Environmental Criteria,

Tianjin Key Laboratory of Environmental Technology for Complex Trans-Media Pollution,

Tianjin Advanced Water Treatment Technology International Joint Research Center,

College of Environmental Science and Engineering, Nankai University, Tianjin 300350, China

Carbon Neutrality Interdisciplinary Science Centre, College of Environmental Science and Engineering, Nankai University, Tianjin 300350, China

⁎ Corresponding author. Tel/Fax: +86 022 23501117. E-mail address: zhoumh@nankai.edu.cn (M. Zhou), nkwangwei@126.com

Note:

- Our responses to the reviewers' comments are shown in color blue.

- All actions of editing taken are shown in color red.

- The line numbers referred correspond to those in the revised manuscript.

Reviewer #1:

In this work, the authors constructed different ultrahigh metal loading single atom catalysts by using a facile one-step calcination. Systematic investigation confirms that the powerful ligand-chelation between oxalic acid and metal ions, as well as the simultaneously generated entangled polymer networks are crucial for achieving high-loading SACs. The results in this manuscript are interesting, but these are some issues in structure and DFT calculations. Thus, I would like to recommend the acceptance of this manuscript for the publication in Nature Communication after addressing the following issues.

Response to Reviewer #1

We sincerely appreciate the thoughtful questions and valuable suggestions raised by the reviewers to improve the manuscript. Below we provide detailed responses to each query, and the corresponding revisions have been incorporated into the manuscript.

Comment 1. The synthesis of ultrahigh metal loading single atom catalysts has not been extensively explored in this work. There is a lack of detailed describe in experimental section, which are very difficult to repeat for readers.

I) What is the sequence of adding MA, OA, and $Fe(NO_3)_3 \cdot 9H_2O$ to deionized water? Will different addition sequences affect the final synthesis of the catalyst?

II) What is the intensity of stirring for the mixed solution, and is it stirred at room temperature?

III) How are the products collected? Is centrifugation involved, and is washing required with H_2O or other solvents?

IV) Is it necessary for the precursor to undergo thorough grinding before calcination?

V) What are the respective amounts of $Fe(NO_3)_3 \cdot 9H_2O$ added during the synthesis process of single-atom Fe with different metal loading?

VI) Why are other chelating ligands used in the synthesis process of single-atom Ag and La? What are the criteria for selecting chelating ligands in different single-atom synthesis processes?

Response:

We appreciate the reviewer's insightful comments regarding the criticality of the synthesis sequence, and the emphasis on operational details. In our protocol:

I) The sequence of adding MA, OA, and $Fe(NO_3)_3 \cdot 9H_2O$ to deionized water does not affect the final synthesis of the catalyst.

II) The resulting mixture was stirred at 500 rpm using a magnetic stirrer at room temperature and maintained for 4 hours.

III) The product was collected by centrifugation and does not require washing.

IV) The centrifuged product was dried at 60°C, thoroughly ground, and

subsequently calcined in a tube furnace under an argon atmosphere.

V) In the synthesis of SACs with distinct metal loadings (5.16 wt%, 15.82 wt%, 24.62 wt%, and 41.31 wt%), fixed quantities of MA (30 mmol) and OA (30 mmol) were employed, while the amounts of $Fe(NO_3)_3 \cdot 9H_2O$ precursor were 0.3 mmol, 0.75 mmol, 0.9 mmol and 1 mmol, respectively.

VI) The crux of our proposed cascade anchoring-directed assembly strategy lies in the selection of chelating ligands with dual functions: (1) coordinating with metal ions to form complexes, and (2) co-assembling with MA to construct macromolecular organic frameworks. This dual functionality enables precise immobilization of metal ions within the growing framework.

Although OA (oxalic acid) exhibits effective chelation with most transition metals, its coordination ability with noble metals (e.g., Ag) and rare-earth metals (e.g., La) is limited, potentially inhibiting the formation of framework. Therefore, we employed CA (citric acid) as an alternative ligand, which shares key characteristics with OA:

- Both are bidentate ligands
- Both can undergo reactive assembly with MA to generate frameworks

Besides，CA has distinct metal coordination selectivity and can preferentially bind with noble/rare-earth metals.

The experimental details and selection criteria for chelating ligands have been supplemented in the revised manuscript (Lines 835-844 and 848-852) as follows:

Specifically, 30 mmol of MA, 30 mmol of OA, and 1 mmol of $Fe(NO_3)_3 \cdot 9H_2O$

were dissolved in deionized water, and the resulting mixture was stirred at 500 rpm using a magnetic stirrer for 4h at room temperature. The product was collected by centrifugation, dried in a 60℃ oven for 24 hours, and thoroughly ground into a homogeneous powder. The obtained catalyst precursor powder was annealed at 550℃ for 2 h under argon atmosphere to obtain Fe-SAC-x (where x referred to the Fe mass fraction in catalyst) at a heating rate of 5℃ min^{-1}. Under the same conditions, Fe-SAC-x with different Fe mass fractions were prepared by adjusting the amount of iron salts (0.3 mmol, 0.75 mmol, 0.9 mmol and 1 mmol, respectively).

The chelating ligand selected for cascade anchoring-directed assembly should not only be able to coordinate with metal ions to form complexes, but also be able to co-assemble with MA to construct macromolecular organic frameworks, thereby achieving precise immobilization of metal ions within the framework. OA can effectively chelate with transition metals, while citric acid (CA) preferentially coordinates with noble/rare-earth metals. Therefore, the synthesis of Mn-SAC, Ag-SAC and La-SAC is similar to that of Fe-SAC, except that Mn ions are still ligand chelated with OA, while Ag and La are ligand chelated with CA.

Comment 2. The results of FTIR suggest that the chelation of Fe^{3+} with OA did not change the skeleton structure, while the results of XRD and Raman demonstrate that the high-loading Fe atoms significantly altered the skeletal structure of the CN substrate. Please provide the more detailed explain.

Response:

We sincerely appreciate the reviewer's insightful observation of the apparent discrepancy between FTIR and XRD/Raman results. Below we provide a refined clarification:

FTIR Analysis (Unchanged Framework): Refers to the supramolecular organic framework formed by OA-MA polymerization prior to pyrolysis. The chelation of Fe^{3+} does not alter the hydrogen-bonded architecture of this precursor, as confirmed by the retained characteristic N-H/O-H vibrational mode (Fig. 2b).

XRD/Raman Shifts (Altered Structure): Characterize the final single-atom catalyst after pyrolysis. High Fe loading induces:

- N-Coordination Occupation: Fe atoms preferentially anchor at the N site, disrupting the long-range order of the CN substrate (evidenced by the gradual disappearance of XRD characteristic peaks, Fig. 1g).
- High content of metal components accelerates the decomposition of carbon nitride during catalytic pyrolysis (Supplementary Fig. 5), creating defective domains (Raman spectral band shift, Supplementary Fig. 2).

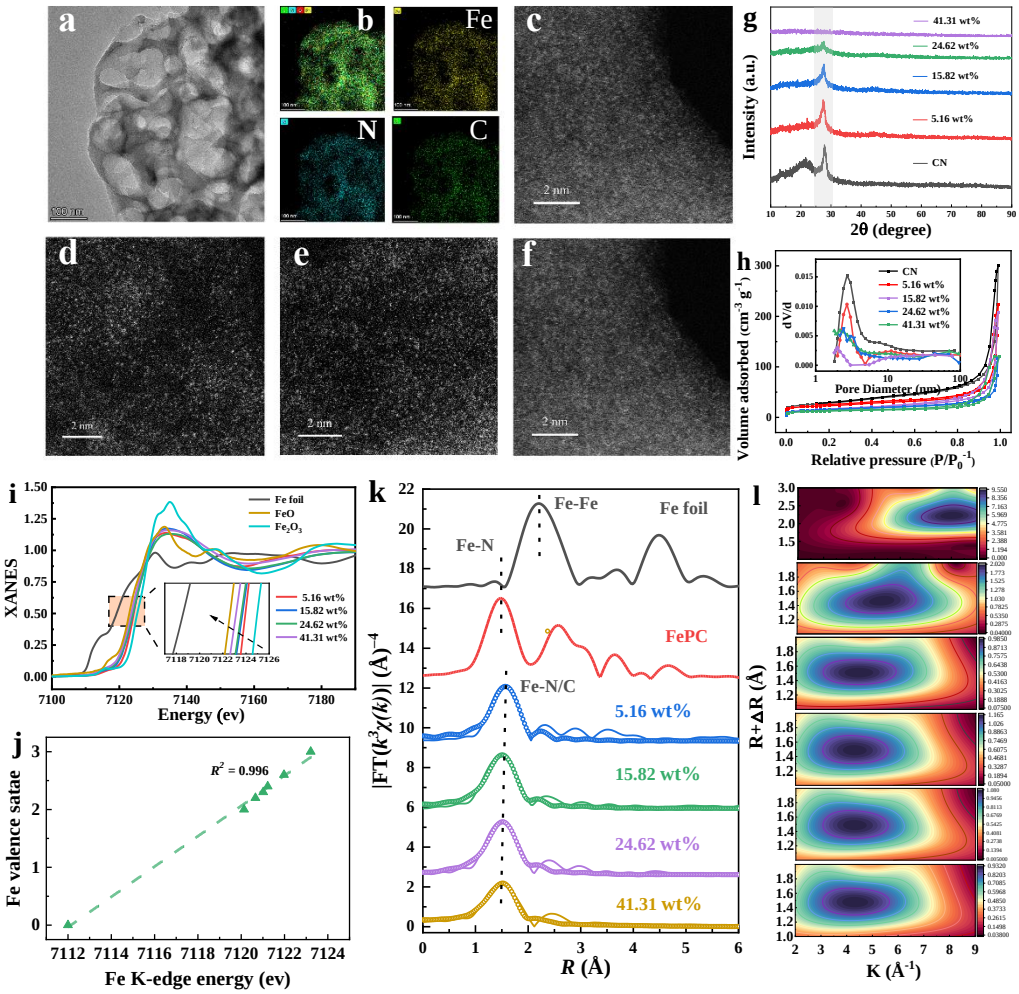

Fig. 1 | Structural characterizations of Fe-SAC-x. a-b, HRTEM and elemental mappings of Fe-SAC-41.31. c-f, HAADF-STEM images of Fe-SAC-x with metal loads was 41.31 wt%, 5.16 wt%, 15.82 wt% and 24.62 wt%, respectively. g, X-ray diffraction (XRD) patterns of as-prepared Fe-SAC-x. h, N_2 sorption isotherms and pore size distribution (inset) for iron-anchored catalysts with different iron loadings. i, Normalized XANES spectra of Fe-SAC-x samples. j, The oxidation state of iron decreased with the increase of metal loading. k, k^3-weighted Fourier transforms. l, wavelet transform of the experimental EXAFS spectra of the indicated catalysts.

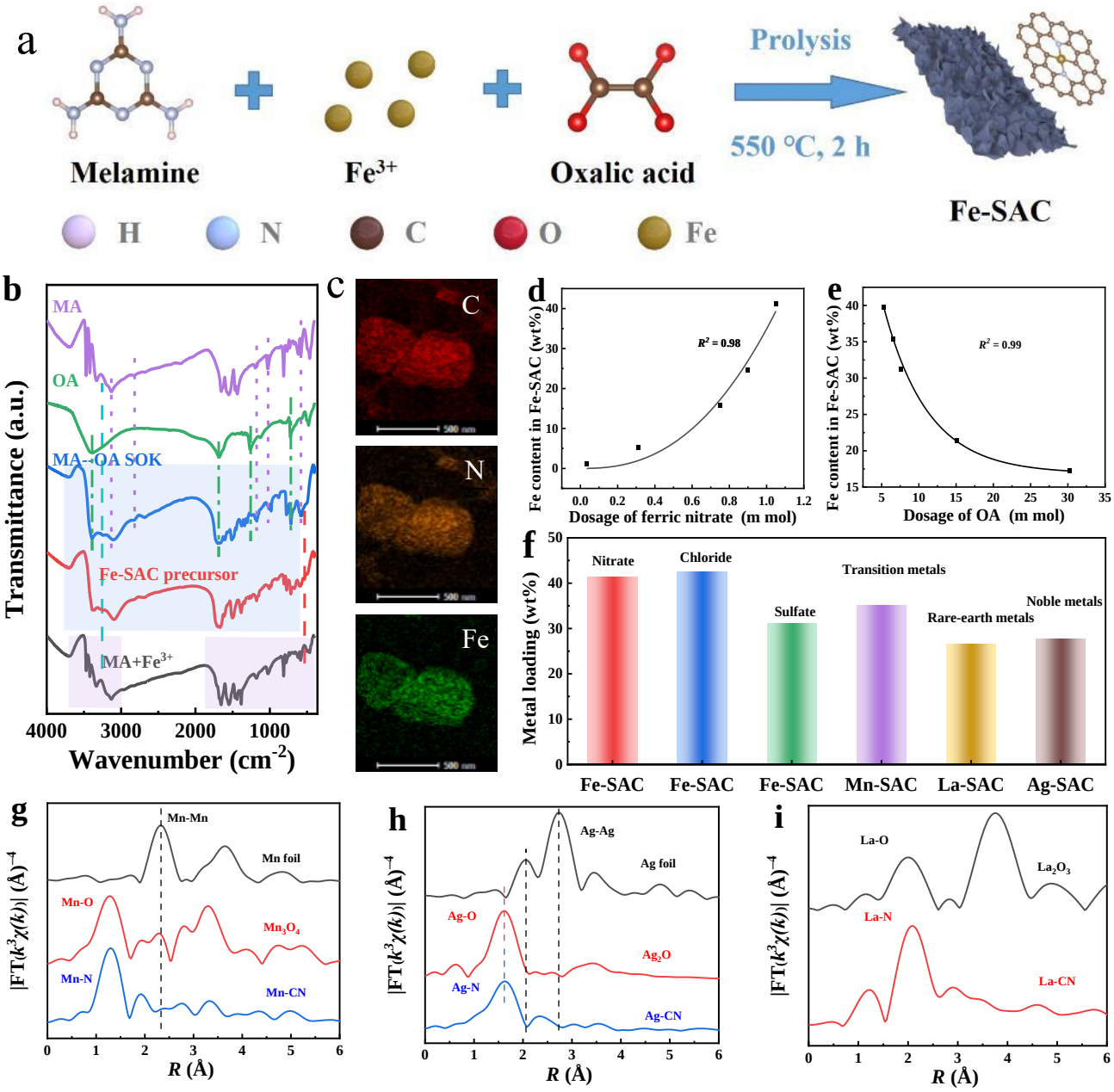

Fig. 2 | Schematic illustration of cascade anchoring strategy for controllable preparation of SACs with ultrahigh metal loadings. a, Schematic synthesis process for Fe-SAC-x catalyst with high Fe loading. b, Fourier transformed infrared (FTIR) spectra of catalyst precursors. c, Elemental mappings of Fe-SAC precursor obtained by the cascade anchoring strategy. d, Linear fitting relationship between SA wt% and metal

salt dosage. e, Linear fitting relationship between SA wt% and OA dosage. f, The metal loading of SAC prepared using different metal salts (nitrate, chloride or sulfate) and metal types (transition, rare-earth or noble metals). g-i, Fourier transform of K-edge EXAFS spectra of Mn-SAC, Ag-SAC and La-SAC, respectively.

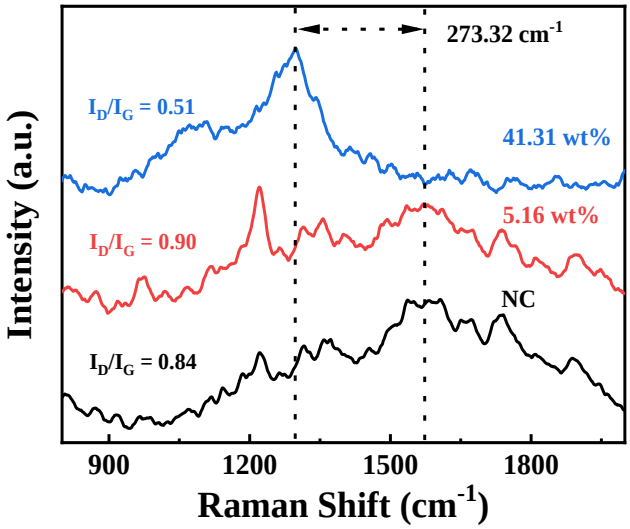

Supplementary Fig. 2 | Raman spectra of as prepared catalysts with different Fe loading.

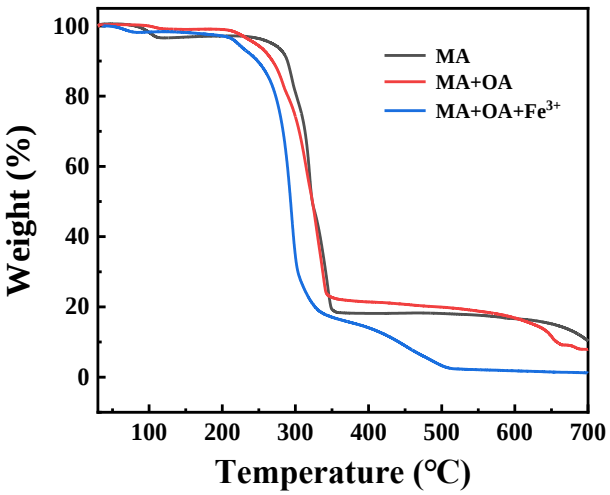

Supplementary Fig. 5 | Thermogravimetric curves of MA, MA+OA supramolecular organic skeleton and Fe-SAC precursor.

To eliminate ambiguity, we have explicitly differentiated between "Fe-SAC precursor" and " the final prepared SAC" in the revised manuscript. There is now an updated statement:

Textual Revisions:

(Lines 153-155): It is worth noting that the signal intensities decreased and eventually disappeared with the increase of metal loading of the pyrolyzed catalyst, suggesting that the highly loaded monatomic metals disrupted the native structure of CN.

(Lines 255-261): The spectrum of the Fe-SAC precursor perfectly matched that of the supramolecular polymer framework, demonstrating that the chelation of Fe^{3+} with OA did not disrupt the skeleton structure. In stark contrast, the precursor prepared by the solvent evaporation method (Supplementary Fig. 3c) displayed a spectrum nearly identical to that of pure MA, with no detectable Fe-O bonding peaks (Fig. 2b), confirming only physical adsorption of Fe^{3+} onto MA.

(Lines 280-282): The synthesis process of SAC through pyrolysis of Fe-SAC precursor was monitored by thermogravimetric analysis (TGA) (Supplementary Fig. 5).

These revisions strengthen the discussion of mechanisms while maintaining consistency with experimental data. We thank the reviewer for prompting this critical clarification.

Comment 3. In Supplementary Fig. 4, the Fe 2p spectra seemingly not shifted towards lower binding energies with increasing Fe loading.

Response:

We sincerely appreciate the reviewer's sharp observation and apologize for the insufficient clarity in our original graphical representation. To address this issue, we have:

I) Re-analyzed the XPS data, and performed full-spectrum charge correction using the adventitious carbon C 1s peak (284.8 eV) (Supplementary Fig. 9).

II) Re-optimized the peak fitting parameters of all Fe-SAC-x catalysts (Supplementary Fig. 10).

III) Confirmed the trend of changes in binding energy.

The Fe 2p 3/2 peak positions systematically shift towards lower binding energies (711.2 → 710.5 eV) as the Fe loading increases from 5.16 to 41.31 wt%. To emphasize this progression, vertical dashed reference lines have been added to the spectra in the revised figure.

Revised Figure:

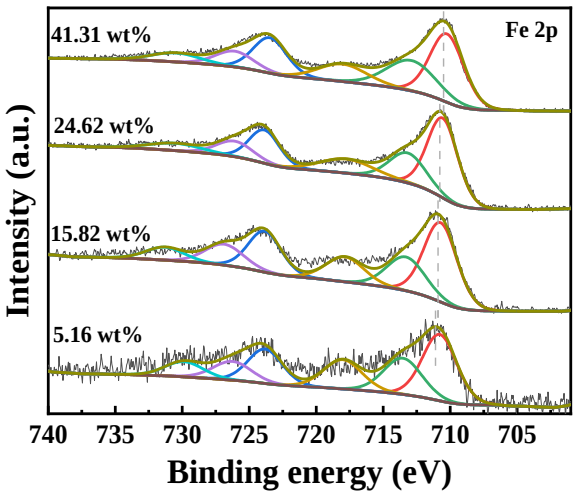

Supplementary Fig. 10 | Fe 2p XPS spectra of Fe-SAC-x (x = 5.16–41.31 wt%).

These revisions unambiguously substantiate the loading-dependent electronic structure modulation. We thank the reviewer for prompting this critical refinement.

Comment 4. As you mentioned, in the process of preparing high-density Fe single atoms, O plays a more crucial role than N, where N functions in coordinating with Fe. What role does O play in this process? Why does O fail to play a similar role in traditional methods of preparing Fe single atoms? The role of O in Fe single atom structure should also be reflected in DFT calculations.

Response:

We sincerely thank the reviewer for raising this critical question regarding the distinct roles of oxygen (O) and nitrogen (N) in our high-density Fe-SAC synthesis. Below we provide a systematic clarification.

From the XPS elemental content analysis, we found that an abnormal increase in O content does occur when preparing highly loaded SACs (Supplementary Table 5).

This may be related to the preferential coordination of metals with O at low temperatures and the substitution of coordinated O atoms by C or N at high temperatures. This phenomenon is very similar to the study of Han et al [1]. They found that the metal loadings have a positive correlation with the O content in SACs, which is a general principle. This finding suggests that oxygen content might play a more important role in controlling SA loading than nitrogen content. Through in-situ XAFS and in-situ XPS together with temperature-dependent thermogravimetric analysis, they investigated the convoluted roles of oxygen and nitrogen in anchoring SAs. The evolution dynamics of SACs synthesis illustrate that the center metal atoms coordinate with O at low temperatures (less than 200℃), and the coordinated O is successively replaced by N or C at high temperatures (400-600℃), and the final coordination environment of SACs depends on not only the SA species but also the terminal temperature.

A similar effect is rarely observed in traditional methods, as in most carbon-based SA systems, oxygen quickly evaporates at 800℃ or above [2]. If SAC is synthesized at high temperatures, it is unlikely to reveal the positive correlation between SA loading and oxygen. It is also important to note that correlation does not mean causality.

Based on the above reasons, at our moderate pyrolysis temperature (550℃), N/C atoms progressively replace the initial Fe-O coordination formed during the low-temperature precursor assembly. So that Fe K-edge EXAFS analysis confirms the exclusive Fe-N/C first-shell coordination (R-space fitting in Fig. 1k) without residual Fe-O bonds (wavelet transform of the experimental EXAFS spectra in Fig. 1l). In

addition, our DFT models prioritize the first-shell coordination because the dominant electronic modulation of Fe 3d orbital hybridization occurs primarily with the nearest-neighbor N/C [3, 4]. The second-shell or bulk O atoms (distance from Fe >3.2 Å) exhibit negligible charge transfer, and the electronic interaction between this non-coordinated O and Fe sites is minimal [5]. To elucidate the critical effects of metal-loading-dependent inter-site spacing variations on the electronic structure of active centers, we primarily focused on the first coordination shell elements of Fe.

Textual Revisions:

(Lines 369-375): However, with the increase of Fe loading, the content of elemental oxygen showed an overall increasing trend, suggesting that oxygen content might play an important role in controlling SA loading. Han et al pointed out that during the formation of highly loaded single atoms, the center metal atoms coordinate with O at low temperatures (less than 200℃) first, and the coordinated O is successively replaced by N or C at high temperatures (400-600℃) [1]. Thus, the coordination environment of metal atoms is closely related to the terminal temperature.

Comment 5. In the DFT calculation process, are the structure models of Fe single atoms with different densities used the same as those presented in Supplementary Figs. 7-10? How are such large models computed using VASP? The raw data (include the initial structure files) from the calculation process should be provided to enable readers to replicate the work.

Response:

We sincerely appreciate the reviewer's suggestion for improving computational transparency. Supplementary Figs. 7-10 in the original manuscript correspond to Supplementary Figs. 13-16 in the revised manuscript.

The structural models in Supplementary Figs. 13-16 represent 5×5 enlarged versions of the core computational unit cell used in DFT calculations (See the green area in Supplementary Figs. 13-16). This scaling was implemented to accurately correlate the theoretical Fe site density with the experimentally measured mass loadings (5.16–41.31 wt%). In addition, the raw data (atomic coordinates of optimized computational models for different metal loading) was provided in Supplementary Data 1.

To eliminate potential ambiguity for readers, we have systematically revised the captions of Supplementary Figures 13-16 and clarified the corresponding methodology descriptions in Lines 383-394 of the revised manuscript, as detailed below:

Revised manuscript：

Lines 384-395: In order to theoretically better understand the effect of metal loading on the electronic structure of Fe atoms, different numbers of Fe sites were uniformly embedded into the same 4×8 graphene cells to represent different metal-loaded Fe-SAC (The green area in Supplementary Figs. 13-16). Such a grid region accommodates 1, 3, 4, and 8 Fe-C1N3 sites, respectively. The calculated theoretical mass loading in the enlarged models is 6.66 wt%, 18.43 wt%, 23.59 wt% and 40.68 wt% (Supplementary Fig. 13-16), which is very close to the actual Fe mass loading of 5.16 wt%, 15.82 wt%, 24.62 wt%, and 41.31 wt% measured by ICP. These models with

different numbers of Fe-C1N3 sites can reliably represent Fe-SACs with different mass loadings for theoretical studies, which is an important guideline for exploring the interactions between Fe sites and constructing efficient SACs.

Revised Figure:

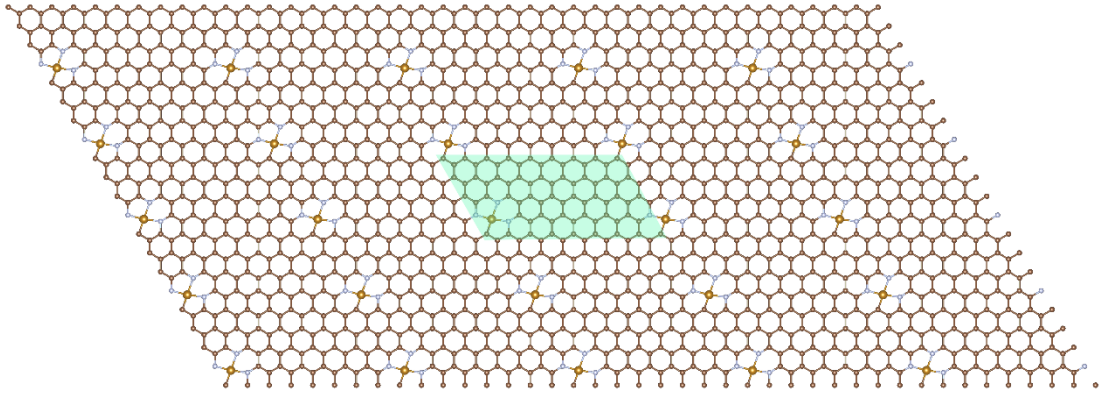

Supplementary Fig. 13 | The scaled-up structure model of Fe-SAC-5.16. The core computing unit cells used in DFT calculations were the green area.

Sample: Fe-SAC-5.16

Number of atoms: 25 Fe, 75 N, 1546 C

Theoretical Fe loading: $Fe(wt\%)=\frac{25\times56}{25\times56+75\times14+1546\times12}=6.66wt\%$

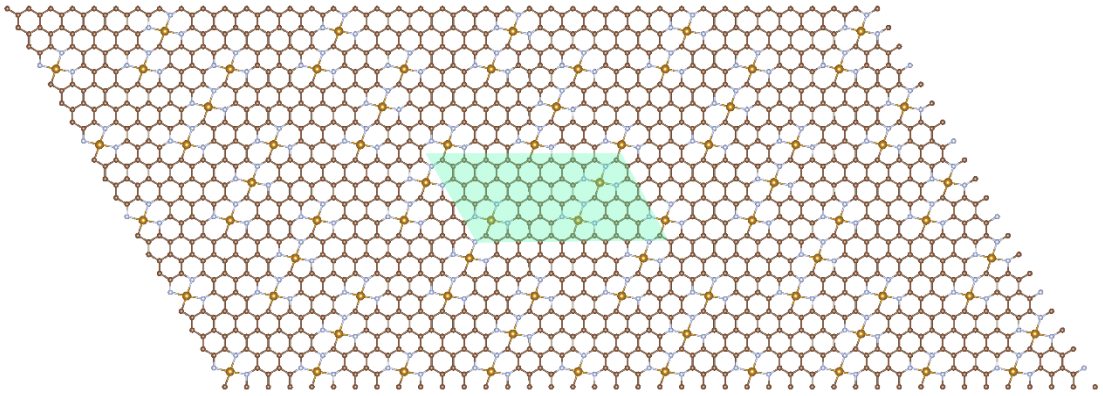

Supplementary Fig. 14 | The scaled-up structure model of Fe-SAC-15.82. The core computing unit cells used in DFT calculations were the green area.

Sample: Fe-SAC-15.82

Number of atoms: 75 Fe, 225 N, 1286 C

Theoretical Fe loading: $Fe(wt\%)=\frac{75\times56}{75\times56+225\times14+1286\times12}=18.43wt\%$

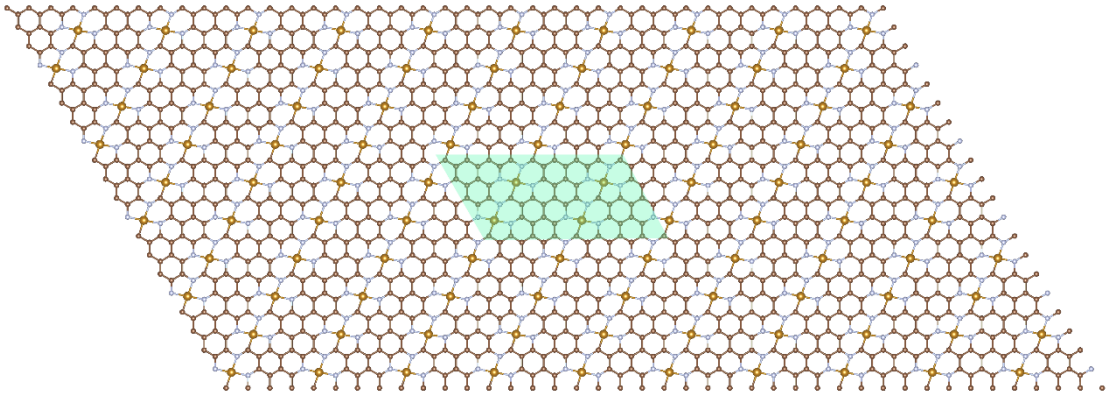

Supplementary Fig. 15 | The scaled-up structure model of Fe-SAC-24.62. The core computing unit cells used in DFT calculations were the green area.

Sample: Fe-SAC-24.62

Number of atoms: 100 Fe, 300 N, 1161 C

Theoretical Fe loading: $Fe(wt\%)=\frac{100\times56}{100\times56+300\times14+1161\times12}=23.59wt\%$

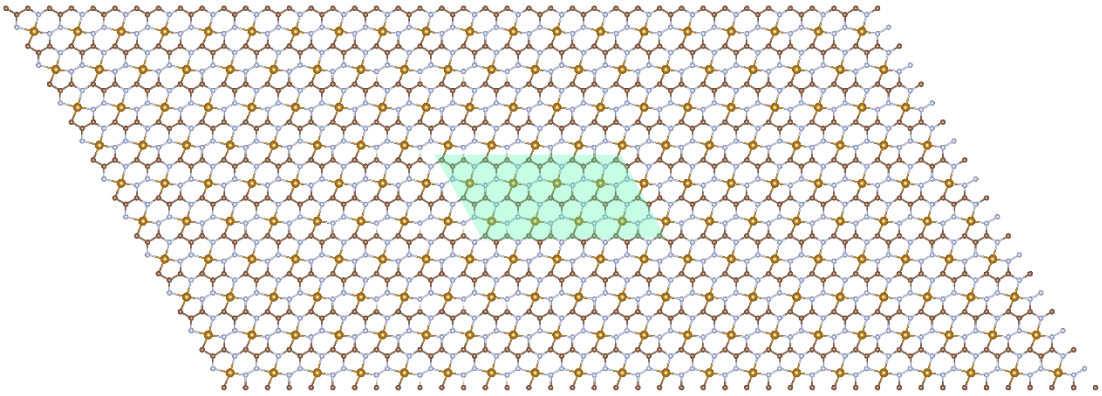

Supplementary Fig. 16 | The scaled-up structure model of Fe-SAC-41.31. The core computing unit cells used in DFT calculations were the green area.

Sample: Fe-SAC-41.31

Number of atoms: 200 Fe, 600 N, 661 C

Theoretical Fe loading: $Fe(wt\%)=\frac{200\times56}{200\times56+600\times14+661\times12}=40.68wt\%$

Comment 6. In supplementary Fig. 11, is the dashed lines representing the position of the Fermi level? Unless specifically stated, the Fermi level in a DOS plot is generally aligned to the zero position. And the PDOS diagrams in supplementary Fig. 11 do not clearly demonstrate the overlap of the 3d orbitals of Fe atoms and the 2p orbitals of N/C atoms increases sequentially with increasing Fe loading. The contribution of Fe 3d orbitals to the pDOS near the Fermi level also do not obvious increases.

Response:

We sincerely appreciate the reviewer's insightful comments on electronic structure analysis. In response to these valuable suggestions, we have implemented the following substantial improvements.

I) Fermi level clarification:

The explicit labeling of Fermi level (dashed line at 0 eV) has been added in the revised Supplementary Fig. 17.

Based on DFT+U, we have re-optimized all catalyst models and re-explored their electronic structures. The detailed DFT+U parameter settings have been incorporated in the quantum chemical calculations section of Supplementary information.

II) Electronic interaction evolution:

The projected density of states (PDOS) calculations elucidate the potential electronic interactions between metal atoms and the support. At higher loading levels, the overlap between the Fe 3d and C/N 2p orbitals decreases, accompanied by slight elongation of Fe-C and Fe-N bond lengths. Furthermore, as the loading increases, the

d-band center of Fe atoms shifts negatively and gradually moves away from the Fermi level, which is consistent with the Bader charge analysis results. These evidences demonstrate that enhanced single-atom loading optimizes the proximity of adjacent single-atom sites, potentially inducing long-range Fe-Fe interactions between neighboring Fe atomic positions. Such long-range interactions modulate the electronic structure and orbital hybridization between Fe atoms and coordinated atoms, while possibly optimizing the adsorption/desorption kinetics of reactive species at active sites. Therefore, tailoring the density of metal site can facilitate electronic structure regulation and promote efficient electron transfer through improved hybridization and bonding interactions between metal atomic orbitals, which may influence the catalytic performance.

Textual Revisions:

(Lines 396-417): Notably, the evolution of coordination environment occurred with the increase of metal loading. Specifically, the Fe-N/C bond lengths increase from 2.08 Å (5.16 wt%) to 2.13 Å (41.31 wt%) (Supplementary Table 6), reflecting the weakening of local hybridization. Meanwhile, PDOS analysis shows diminished overlap between Fe 3d and C/N 2p states at higher loadings (Supplementary Fig. 17). This reduction in orbital overlap corroborates the structural relaxation observed in bond lengths. It is worth noting that long-range electronic coupling was observed through the d-band shift. The Fe d-band center shifts negatively from −1.51 eV to −2.72 eV relative to the Fermi level as the loading increases, indicating enhanced metal-support charge transfer [6], which is consistent with the analysis results of bader charge (Supplementary

Table 6) and charge density difference (Supplementary Fig. 18). These findings demonstrate that an increase in single-atom loading optimizes the proximity between adjacent Fe sites, inducing long-range Fe-Fe interactions mediated by the support. Such long-range interactions modulate the electronic structure of Fe atoms and the hybridization of atomic orbitals with coordinated atoms, thereby optimizing the adsorption/desorption kinetics of reactive intermediates. Specifically, the downshifted d-band weakens the intermediate binding strength, while the enhanced electron transfer kinetics through long-range coupling may improve catalytic efficiency, as evidenced by the reduced R_{ct} in EIS below (Fig. 3d). Consequently, tailoring metal site density enables precise electronic structure modulation and facilitates efficient electron transfer through improved hybridization and bonding interactions between metal atomic orbitals, ultimately influencing catalytic performance.

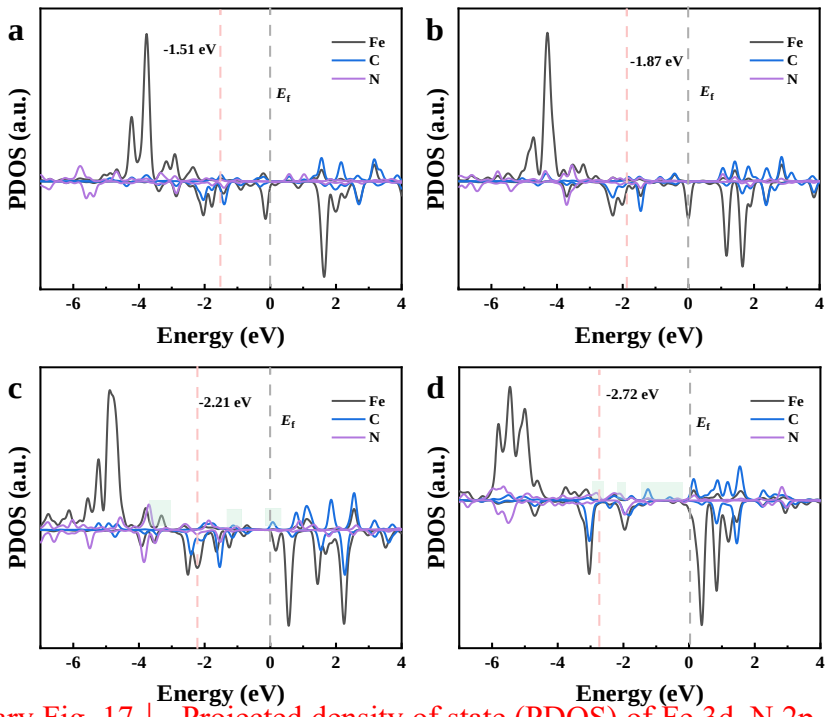

Supplementary Fig. 17 | Projected density of state (PDOS) of Fe 3d, N 2p, and C 2p

orbital of Fe-SAC-5.16 (a), Fe-SAC-15.82 (b), Fe-SAC-24.62 (c) and Fe-SAC-41.31 (d), respectively.

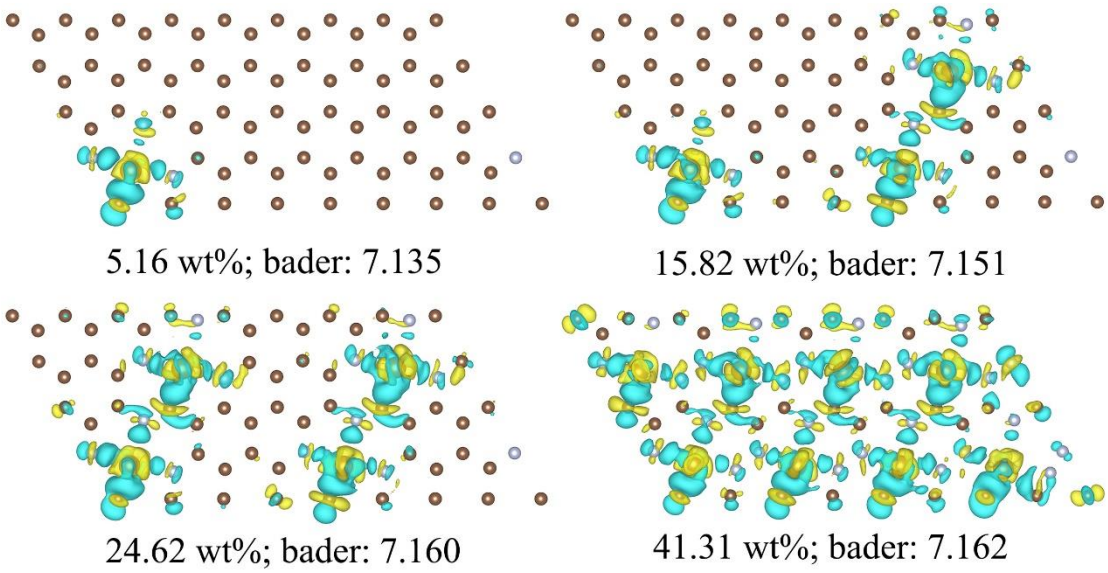

Supplementary Fig. 18 | Differential charge density of Fe–SAC-x models.

Supplementary Table 6 | Fe coordination bond lengths and bader charges under different loads.

Sample	Fe-C (Å)	Fe-N (Å)	Bader (Fe)
Fe-SAC 5.16 wt%	1.623	2.024	7.135
Fe-SAC 15.82 wt%	1.632	2.033	7.151
Fe-SAC 24.62 wt%	1.640	2.054	7.160
Fe-SAC 41.31 wt%	1.657	2.087	7.162

These revisions significantly strengthen the understanding of structure-property relationship. We are grateful for the opportunity to enhance the scientific rigor of this work through the reviewer's expert guidance.

Comment 7. Due to the strong correlation of d electrons in Fe, the DFT+U is necessary.

Response:

We sincerely appreciate the reviewer's crucial suggestion regarding the treatment of strongly correlated d-electrons. Following your professional guidance, we have systematically implemented the DFT+U methodology and made the following substantial improvements.

I) Standardized DFT+U parameters:

A Hubbard U correction of 3.29 eV was applied to Fe 3d orbitals, which is consistent with benchmark studies of iron-based single atom catalysts [7, 8]. The Dudarev approach was adopted with tightened convergence criteria (10^{-5} eV for electronic steps and 0.01 eV/Å for ionic relaxation). The detailed DFT+U parameter settings have been incorporated in the quantum chemical calculations section of Supplementary information.

II) Comprehensive recalculations:

All key calculations have been re-performed using DFT+U, including:

Confirmation of the coordination configuration of single atom Fe (revised Supplementary Fig.12).

Structural optimization of Fe loading models (revised Supplementary Figs.13-16).

Projected density of state (PDOS) of Fe 3d, N 2p, and C 2p orbital (revised Supplementary Figs.17).

Differential charge density of Fe–SAC-x models (revised Supplementary Figs.18).

In-depth analysis of the electronic structure and coordination environment of Fe sites on catalysts with different loadings, including coordination bond length and bader

charge (Supplementary Table 6).

Adsorption energy of PMS by Fe-SAC-x and the differential charge density, bader charge transfer after the adsorption of PMS by Fe-SAC-x with different Fe loading (revised Fig. 4g).

Energy profiles of $^1O_2$ derived pathways on varying Fe density models (revised Fig. 4h).

III) Textual Revisions

(line 379-416):

Based on the Fe-CN optimization model established by XAFS and XPS, three possible CN coordination modes are considered. As shown in Supplementary Fig. 12, the isolated Fe atom has a more negative binding energy when combined with C1N3 configuration, so this coordination configuration is more stable compared with the others. In order to theoretically better understand the effect of metal loading on the electronic structure of Fe atoms, different numbers of Fe sites were uniformly embedded into the same 4×8 graphene cells to represent different metal-loaded Fe-SAC (The green area in Supplementary Figs. 13-16). Such a grid region accommodates 1, 3, 4, and 8 Fe-C1N3 sites, respectively. The calculated theoretical mass loading in the enlarged models is 6.66 wt%, 18.43 wt%, 23.59 wt% and 40.68 wt% (Supplementary Fig. 13-16), which is very close to the actual Fe mass loading of 5.16 wt%, 15.82 wt%, 24.62 wt%, and 41.31 wt% measured by ICP. These models with different numbers of Fe-C1N3 sites can reliably represent Fe-SACs with different mass loadings for theoretical studies, which is an important guideline for exploring the interactions

between Fe sites and constructing efficient SACs.

Notably, the evolution of coordination environment occurred with the increase of metal loading. Specifically, the Fe-N/C bond lengths increase from 2.08 Å (5.16 wt%) to 2.13 Å (41.31 wt%) (Supplementary Table 6), reflecting the weakening of local hybridization. Meanwhile, PDOS analysis shows diminished overlap between Fe 3d and C/N 2p states at higher loadings (Supplementary Fig. 17). This reduction in orbital overlap corroborates the structural relaxation observed in bond lengths. It is worth noting that long-range electronic coupling was observed through the d-band shift. The Fe d-band center shifts negatively from −1.51 eV to −2.72 eV relative to the Fermi level as the loading increases, indicating enhanced metal-support charge transfer [6], which is consistent with the analysis results of bader charge (Supplementary Table 6) and charge density difference (Supplementary Fig. 18). These findings demonstrate that an increase in single-atom loading optimizes the proximity between adjacent Fe sites, inducing long-range Fe-Fe interactions mediated by the support. Such long-range interactions modulate the electronic structure of Fe atoms and the hybridization of atomic orbitals with coordinated atoms, thereby optimizing the adsorption/desorption kinetics of reactive intermediates. Specifically, the downshifted d-band weakens the intermediate binding strength, while the enhanced electron transfer kinetics through long-range coupling may improve catalytic efficiency, as evidenced by the reduced R_{ct} in EIS below (Fig. 3d). Consequently, tailoring metal site density enables precise electronic structure modulation and facilitates efficient electron transfer through improved hybridization and bonding interactions between metal atomic orbitals,

ultimately influencing catalytic performance.

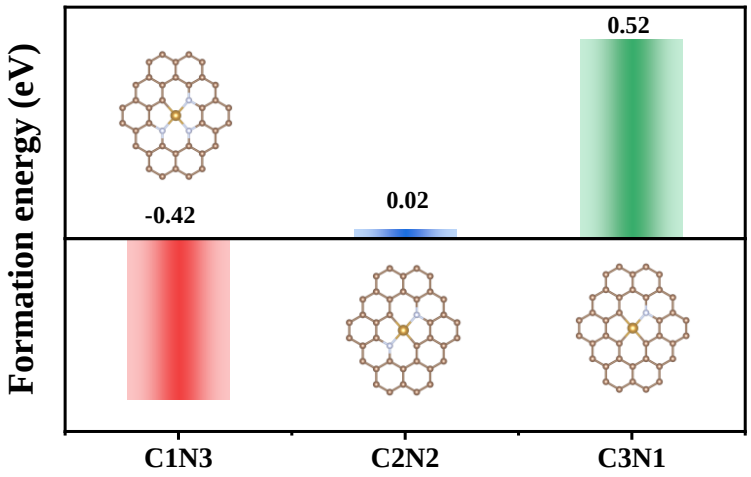

Supplementary Fig. 12 | The binding energies of the possible CN coordination modes.

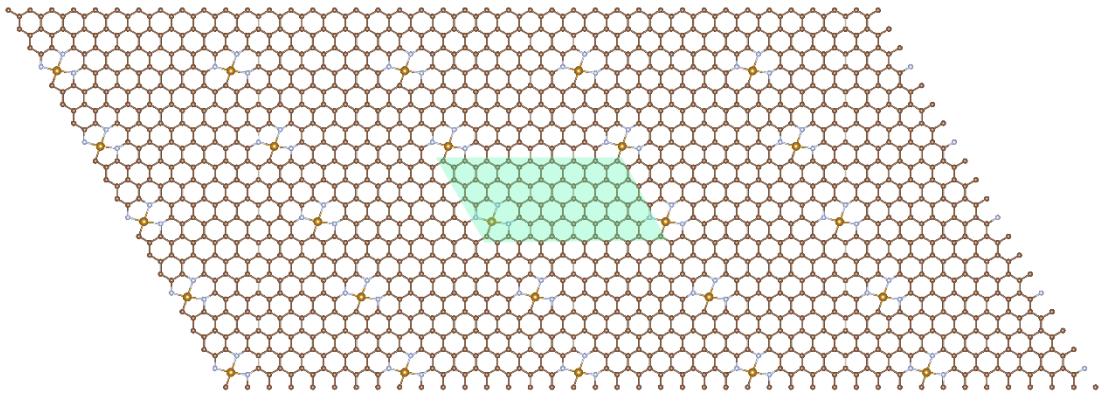

Supplementary Fig. 13 | The scaled-up structure model of Fe-SAC-5.16. The core computing unit cells used in DFT calculations were the green area.

Sample: Fe-SAC-5.16

Number of atoms: 25 Fe, 75 N, 1546 C

Theoretical Fe loading: $Fe(wt\%)=\frac{25\times56}{25\times56+75\times14+1546\times12}=6.66wt\%$

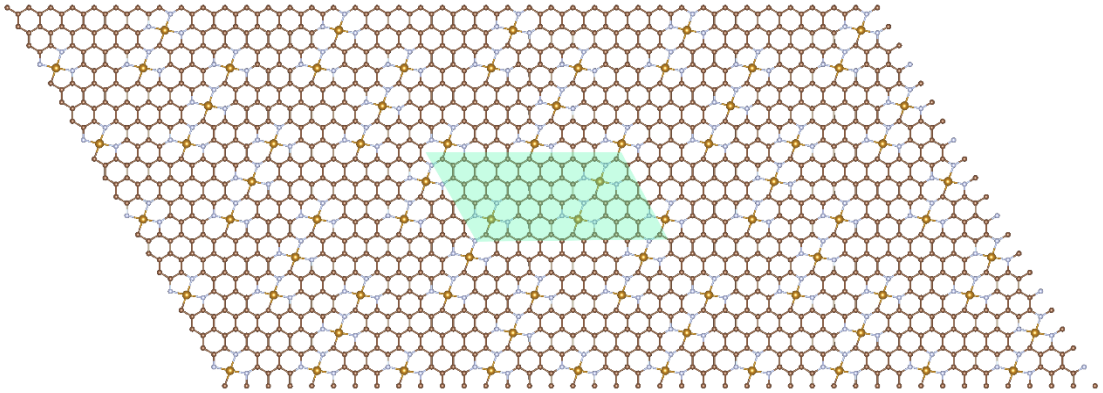

Supplementary Fig. 14 | The scaled-up structure model of Fe-SAC-15.82. The core computing unit cells used in DFT calculations were the green area.

Sample: Fe-SAC-15.82

Number of atoms: 75 Fe, 225 N, 1286 C

Theoretical Fe loading: $Fe(wt\%)=\frac{75\times56}{75\times56+225\times14+1286\times12}=18.43wt\%$

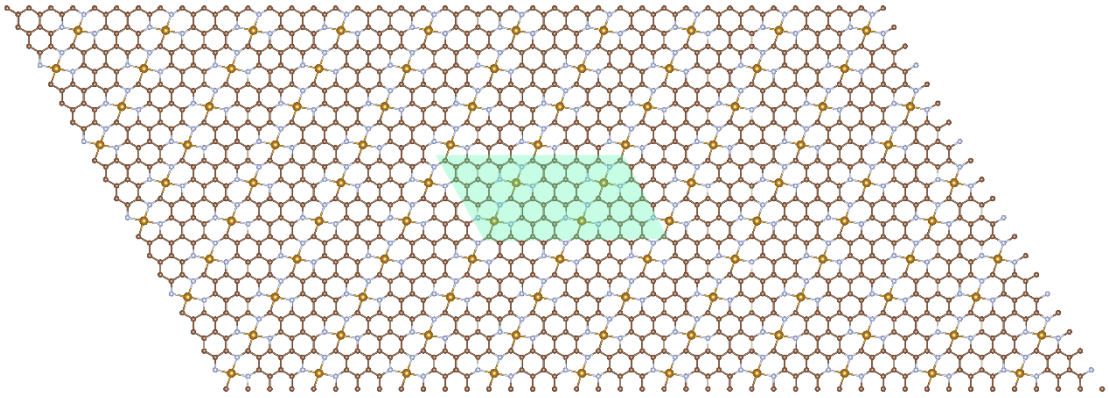

Supplementary Fig. 15 | The scaled-up structure model of Fe-SAC-24.62. The core computing unit cells used in DFT calculations were the green area.

Sample: Fe-SAC-24.62

Number of atoms: 100 Fe, 300 N, 1161 C

Theoretical Fe loading: $Fe(wt\%)=\frac{100\times56}{100\times56+300\times14+1161\times12}=23.59wt\%$

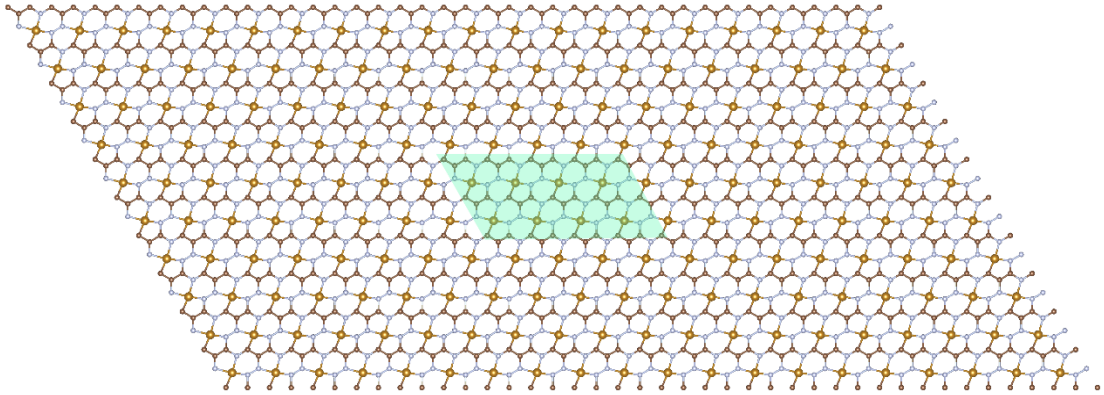

Supplementary Fig. 16 | The scaled-up structure model of Fe-SAC-41.31. The core computing unit cells used in DFT calculations were the green area.

Sample: Fe-SAC-41.31

Number of atoms: 200 Fe, 600 N, 661 C

Theoretical Fe loading: $Fe(wt\%)=\frac{200\times56}{200\times56+600\times14+661\times12}=40.68wt\%$

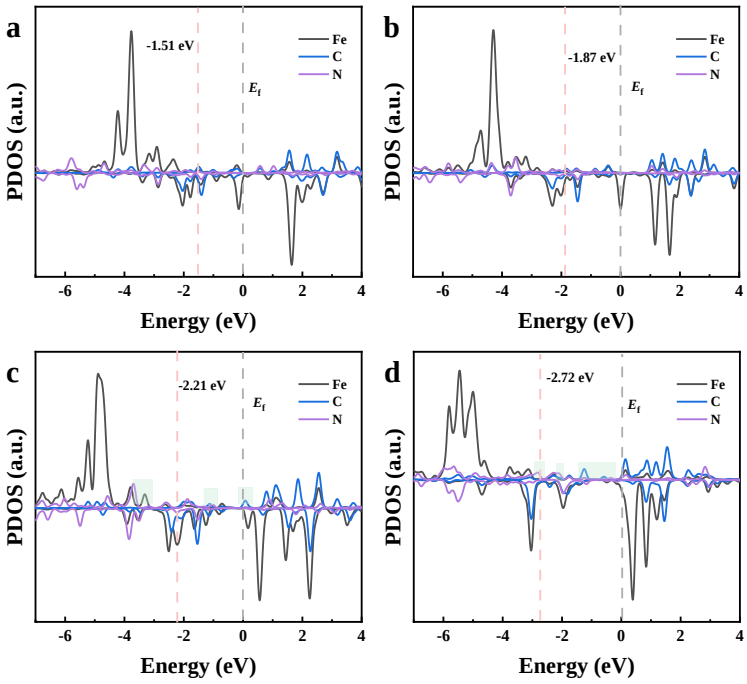

Supplementary Fig. 17 | Projected density of state (PDOS) of Fe 3d, N 2p, and C 2p orbital of Fe-SAC-5.16 (a), Fe-SAC-15.82 (b), Fe-SAC-24.62 (c) and Fe-SAC-41.31 (d), respectively.

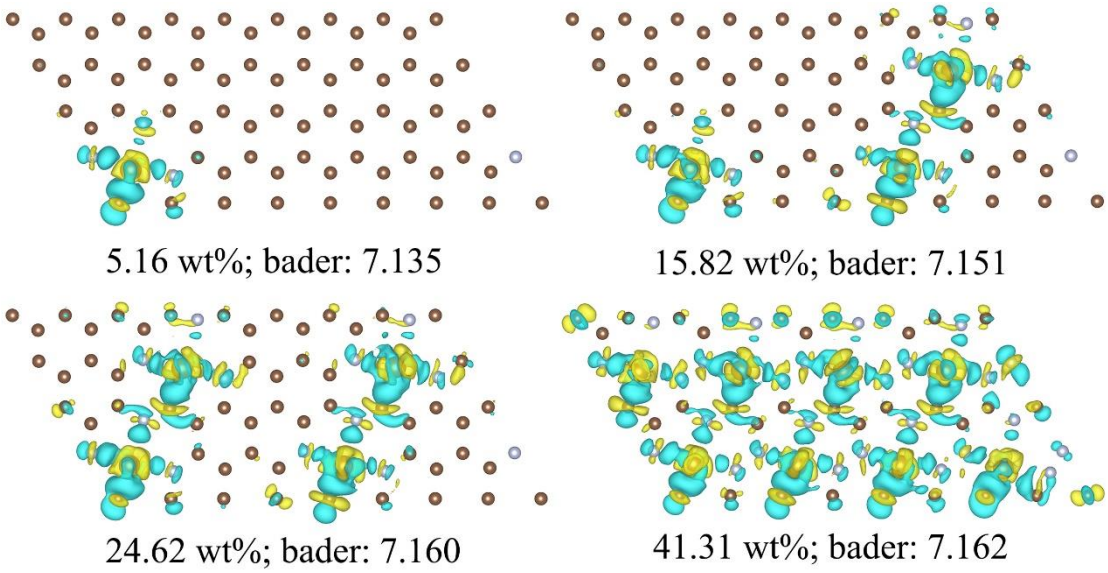

Supplementary Fig. 18 | Differential charge density of Fe–SAC-x models.

Supplementary Table 6 | Fe coordination bond lengths and bader charges under different loads.

Sample	Fe-C (Å)	Fe-N (Å)	Bader (Fe)
Fe-SAC 5.16 wt%	1.623	2.024	7.135
Fe-SAC 15.82 wt%	1.632	2.033	7.151
Fe-SAC 24.62 wt%	1.640	2.054	7.160
Fe-SAC 41.31 wt%	1.657	2.087	7.162

(Lines 661-695):

Notably, Fig. 4f reveals a positive correlation between k and the number of active sites. However, this positive correlation is non-linear, and the catalytic kinetics are significantly accelerated at high loadings. Assuming that each site exhibits similar intrinsic activity, the apparent rate constant k should theoretically display a linear or quasi-linear relationship with the total number of active sites. Combined with the

electronic structure changes of Fe sites at high loadings, it collectively demonstrates the potential existence of long-range Fe-Fe interactions at elevated metal loadings, which enhances the catalytic activity of active sites. In addition, when the metal loading exceeds 24.62 wt%, the evolution of k values accelerates markedly, suggesting the existence of a critical loading threshold beyond which these long-range interactions become significantly enhanced.

To validate the above conclusions, we investigated the PMS catalytic performance at identical Fe active sites in catalyst models with varying metal loadings by DFT. It was observed that the PMS adsorption energy significantly increased when the metal loading reached 24.62 wt%, and as the loading continued to rise, the adsorption energy further changed (Fig. 4g). Additionally, the interaction between Fe sites and PMS exhibited enhanced differentiation due to intermetallic effects. Specifically, the electron depletion region of the Fe adsorption center expanded markedly, while the bonded O atom accumulated more electrons. Bader charge analysis further revealed an increase in electron transfer from isolated Fe atoms to PMS molecules under higher Fe loading (Fig. 4g). This demonstrates that long-range metallic interactions at high loadings facilitate the activation of PMS by Fe site. This result is consistent with the open circuit potential test, indicating that catalysts with higher mass loading triggered higher potential jumps (Fig.4a). Catalysts with higher metal loading simultaneously exhibited lower charge transfer resistance (Fig. 3d), which collectively proves that elevated metal loading is beneficial for promoting the conductive bridging of Fe atoms to facilitate charge migration. Notably, when the metal loading surpassed the critical threshold of

24.62 wt%, the energy barriers of the $^1O_2$ generation pathway and rate-determining step (RDS) decreased substantially (Fig. 4h, $\Delta E_{rds,41.31} = 1.16$ eV $<$ $\Delta E_{rds,24.62} = 1.19$ eV $<$ $\Delta E_{rds,15.82} = 1.47$ eV $<$ $\Delta E_{rds,5.16} = 2.12$ eV). These theoretical analyses, combined with experimental results, including OCP (Fig. 4a), i-t curves (Fig. 4b), and SMX degradation kinetics (Fig. 4f), collectively demonstrate that long-range Fe-Fe interactions are significantly enhanced beyond the critical loading threshold of 24.62 wt%. These interactions play a pivotal role in reducing energy barriers and improving electron transfer efficiency.

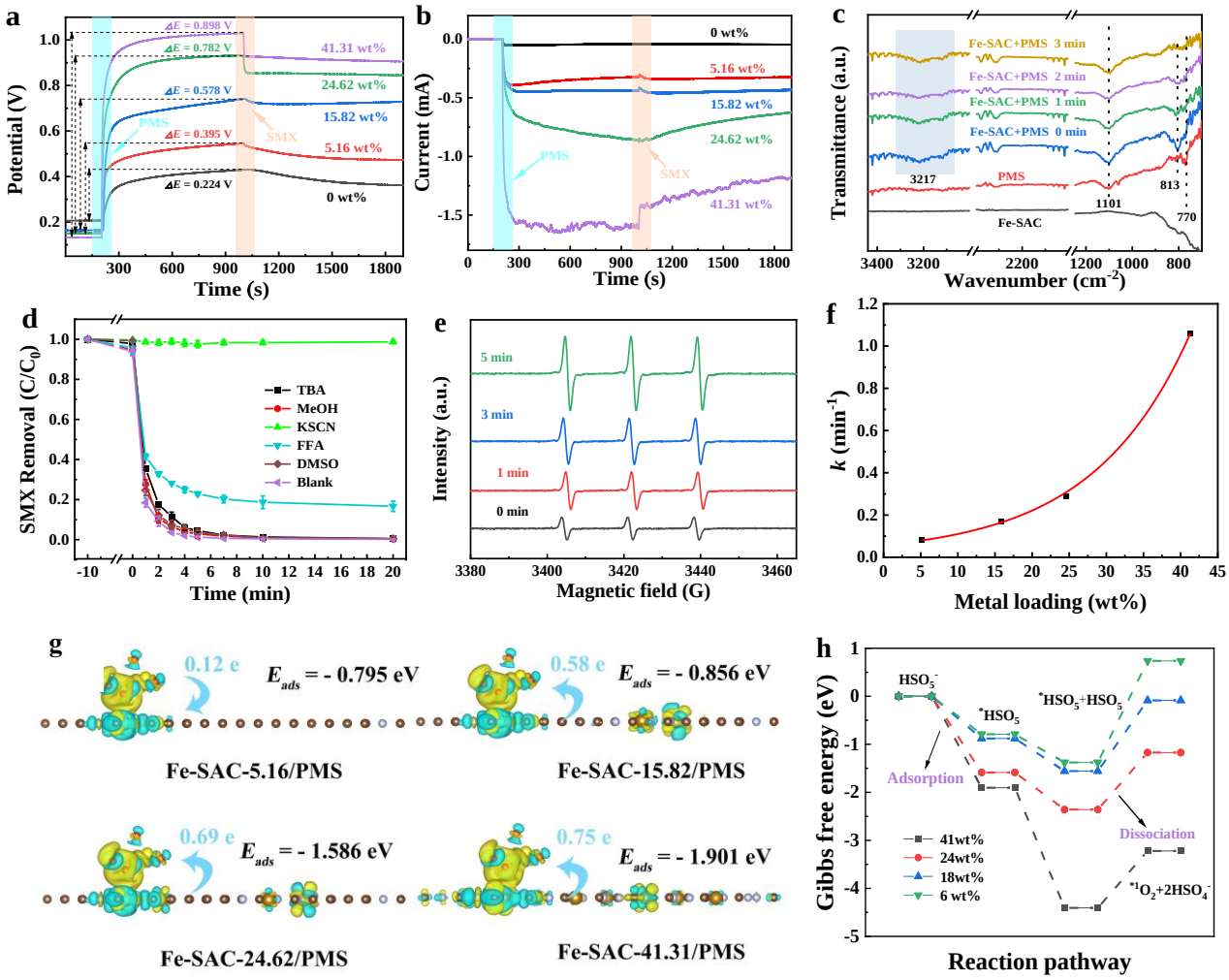

Fig. 4 | Evaluation of catalytic mechanism under gradient metal loading. a, The open-circuit potential changes of Fe-SAC-x when PMS or SMX is added respectively. b, Effects of PMS or SMX addition on the i-t curves at the corresponding open circuit potential. c, In situ FTIR spectra of Fe-SAC, PMS alone, and Fe-SAC combined with PMS. d, Effects of quenching reactive oxygen species on the degradation of SMX. e, Electron paramagnetic resonance spectra of TEMP-$^1O_2$ during SMX degradation in the Fe-SAC-4.31/PMS system. f, The relationship between metal loading and the apparent rate constant (k). g, Adsorption energy of PMS by Fe-SAC-x and the differential charge density, bader charge transfer after the adsorption of PMS by Fe-SAC-x with different Fe loading. h, Energy profiles of $^1O_2$ derived reaction on varying Fe density models.

We greatly appreciate the opportunity to utilize the professional knowledge recommended by the reviewers to enhance the computation in this study, which is crucial for elucidating the structure-property relationships of Fe-based SACs.

Comment 8. The structural characterization and DFT calculations of ultra-high-density single-atom catalysts in this paper need to be refined.

Response:

We sincerely appreciate the reviewer's crucial guidance regarding the refinement of structural characterization and computational methodology for ultra-high-density SACs. In response to these valuable suggestions, we have made comprehensive improvements to the structural characterization (Comment 3) and DFT calculations (Comment 5-7).

Reviewer #2:

The authors present the preparation of highest metal loading to date on carbon nitride, including transition metals (Fe, Mn), rare earth metal (La), and noble metal (Ag) SAC. The mechanism for such high metal loading was systematically studied, and studied the structure-catalysis conformational relationship by the activation of peroxymonosulfate (PMS) for toxic organics degradation. Therefore, I would recommend it to be published after a major revision by addressing the following comments/questions.

Response to Reviewer #2

We sincerely appreciate your recognition of this work's significance and your insightful suggestions for improvement. Your comments have profoundly inspired our understanding of the structure-catalysis relationships in ultrahigh-loading SACs. Below we provide detailed responses to each query, and the corresponding revisions have been incorporated into the manuscript.

Comment 1. In this work, why was carbon nitride chosen as the metal-supporting substrate instead of other high surface area materials (such as graphene, diatomaceous earth, etc.)? What are its advantages?

Response:

We sincerely appreciate the reviewer's insightful inquiry into the substrate selection, which provides an excellent opportunity to clarify the unique advantages of our carbon nitride-based system. The choice of supporting material is indeed a critical consideration in this study, and we are grateful for the chance to elaborate on this design

rationale.

The high surface free energy of metal atoms makes them prone to agglomeration during pyrolysis. Therefore, robust metal-support binding and uniform dispersion play a decisive role in synthesizing high-loading single-atom catalysts. Although materials such as graphene or diatomaceous earth possess high surface areas, existing synthesis methods fail to achieve dense yet discrete distribution of metal atoms on their surfaces. A key limitation lies in the insufficient nitrogen species available to coordinate numerous metal atoms, which inevitably leads to the formation of cluster or nanoparticle during high-loading SAC preparation.

This study selects carbon nitride as the supporting substrate not only because of its abundant nitrogen species, but more importantly, for the employed bottom-up self-assembly strategy. Specifically, oxalic acid, a well-known bidentate ligand, can chelate various metal ions. Crucially, due to the composite reaction between carboxyl and amino groups, oxalic acid reacts with melamine molecules to form a macromolecular organic framework. In our proposed cascade-anchored self-assembly strategy, the chelation of metal ions by oxalic acid and its subsequent composite reaction with melamine enable in-situ anchoring of metal ions into the synchronously formed macromolecular framework via chemical bonding (Fig. 2a-b). This ensures a dense and discrete distribution of metal ions in the catalyst precursor (Fig. 2c), thereby maximizing the utilization of nitrogen species in the substrate during subsequent pyrolysis.

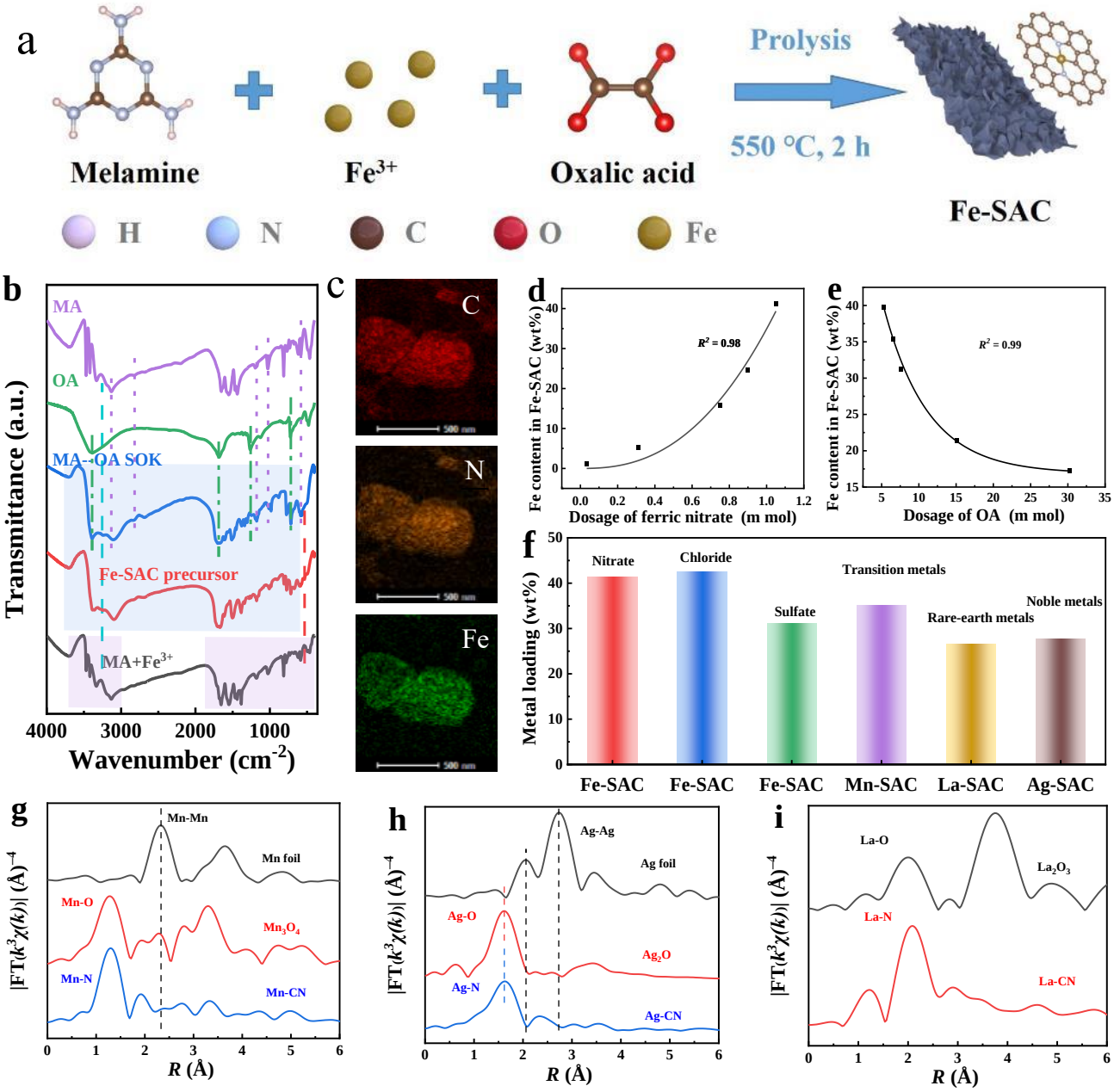

Fig. 2 | Schematic illustration of cascade anchoring strategy for controllable preparation of SACs with ultrahigh metal loadings. a, Schematic synthesis process for Fe-SAC-x catalyst with high Fe loading. b, Fourier transformed infrared (FTIR) spectra of catalyst precursors. c, Elemental mappings of Fe-SAC precursor obtained by the cascade anchoring strategy. d, Linear fitting relationship between SA wt% and metal

salt dosage. e, Linear fitting relationship between SA wt% and OA dosage. f, The metal loading of SAC prepared using different metal salts (nitrate, chloride or sulfate) and metal types (transition, rare-earth or noble metals). g-i, Fourier transform of K-edge EXAFS spectra of Mn-SAC, Ag-SAC and La-SAC, respectively.

Textual Revisions

Lines 225-228:

On the other hand, the full utilization of ligand atoms is another key to achieve high metal loading, which requires chemical control of the metal at the atomic or molecular level to achieve its homogeneous dispersion on the carrier or precursor and to fully occupy the chelation sites of metal.

Lines 232-244:

Carbon nitride (CN) is an excellent carrier of single atoms due to its thermal stability and high content of coordination sites, mainly provided by nitrogen atoms. Although it exhibits the homogeneity of ligand site, the chemical stability of triazine or heptazine unit limits the effective utilization of numerous N sites in CN. Considering this limitation, a bottom-up in-situ assembled cascade anchoring mechanism was adopted in this study.

During the preparation of Fe-SAC precursor, the metal ions are strongly assembled into the supramolecular organic skeleton (SOK) through chemical bonding, and the subsequent high-temperature pyrolysis further anchors the metal atoms in-situ at the nearby N sites. **Fig. 2a** illustrates this simple synthesis strategy. Fe^{3+} was assembled into the SOK of oxalate-melamine macromolecules using OA because it can either

chelate with Fe^{3+} [Eq. (1)] or react with melamine (MA) to form a supramolecular organic framework [Eq. (2)].

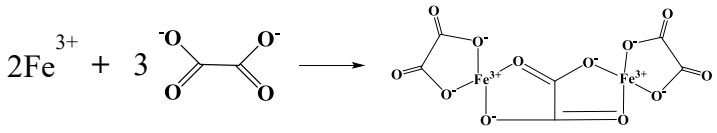

(1)

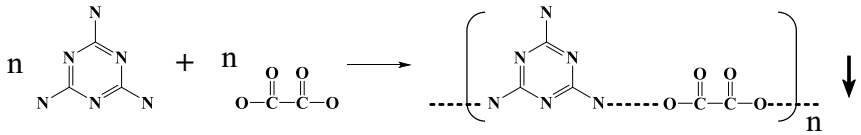

(2)

Comment 2. The acid-base properties significantly affect the catalytic performance of Fenton-like catalysts. The paper only demonstrates that Fe-SAC-41.31/PMS system has strong environmental anti-interference ability for SMX degradation under different acidic environments. Therefore, what is the activity of the catalyst in different alkaline environments?

Response:

We sincerely appreciate the reviewer's insightful suggestion on the alkaline environment evaluation, which significantly strengthens the comprehensiveness of our catalytic performance analysis. Following this valuable guidance, we have systematically investigated the activation performance of PMS under alkaline conditions.

Textual Revisions:

(Lines 489-499):

pH represents a critical determinant of aquatic matrices in practical settings. The initial solution pH fundamentally governs both the interfacial characteristics of

electrocatalytic surfaces and the oxidative capacity of reactive oxygen species. Consequently, pollutant degradation efficiency across varying pH conditions serves as a pivotal metric for evaluating the real-world applicability of water treatment technologies. The Fe-SAC-41.31/PMS system demonstrates exceptional SMX elimination efficacy over an extensive pH spectrum (pH 3–10; **Supplementary Fig. 28**), underscoring its significant potential for practical implementation. This performance stems from the heightened oxidative potential of peroxymonosulfate's anionic species ($^{-}O–O–SO_3^{-}$) relative to its protonated precursor (H_2SO_5), coupled with its susceptibility to base-catalyzed activation [9].

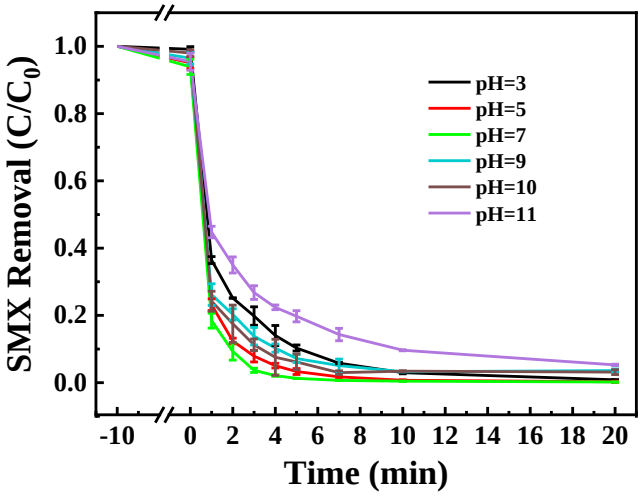

Supplementary Fig. 28 | Degradation performance of SMX at different initial pH. Experimental conditions: $[PMS]_0$ = 2 mM, catalyst: 0.1g L^{-1}.

Comment 3. In this study, the highest metal load in Fe based SAC to date (41.31 wt%) was obtained through a cascading anchoring strategy, and it demonstrated the best catalytic performance. So, what is the loading limit of Fe? Will more loads lead to better catalytic performance?

Response:

During the catalyst preparation, we observed that a maximum metal loading capacity exists when the concentrations of melamine (MA) and oxalic acid (OA) are fixed. Once this limit is reached, further addition of metal salt leads to metal aggregation. Within the loading range used in this study, the activation efficiency of peroxymonosulfate (PMS) and the degradation performance of sulfamethoxazole (SMX) improved consistently with the increase of metal loading. The underlying reasons are elaborated below.

Textual Revisions:

Lines 307-328:

Intriguingly, for the final synthesized SAC, its Fe mass fraction increases nonlinearly with iron salt content in precursors (Fig. 2d). This indicates that a smaller incremental increase in Fe salt injection in the later stage can cause a significant rise in Fe loading. To elucidate this anomalous behavior, we systematically investigated the synthesis process of high-loading Fe-SACs. Given the critical role of OA in coordinating metal ions, the amount of OA added was adjusted while maintaining a fixed concentration of MA and Fe salt. It was found that the OA content significantly influences the yield of Fe-SAC precursor and the ultimate metal loading of SAC (Supplementary Table 4). This demonstrates a concentration-dependent relationship between MA, OA, and Fe^{3+}, and reveals that the supramolecular organic framework possesses a maximum metal loading capacity. Increasing the OA content generates more catalyst substrate (Supplementary Table 4), resulting in a corresponding reduction

in metal loading (Fig. 2e). This counterintuitive phenomenon is the inverse of the trend observed in Fig. 2d, where increasing the Fe salt dosage while keeping MA and OA fixed gradually approaches the maximum loading capacity of the framework, resulting in a rapid surge in metal loading. This systematic investigation reveals that oxalate acts as a "structure-directing agent" that governs framework integrity and metal stabilization capacity, rather than just a sacrificial template. The dosage of Fe^{3+} salt directly controls the loading level. The orthogonal tunability of these two parameters provides exceptional flexibility for SAC design, further underscoring the novelty and practicality of our method.

Supplementary Table 4 | Relationship between OA content, SAC precursor yield, and metal loading of as prepared SAC.

Number	OA (mmol)	SAC precursor yield (g)	SAC	Metal loads (wt%)
1	1.5	/	/	/
2	3.1	0.5305	No	/
3	4.2	0.8135	No	/
4	5.3	1.1324	Yes	39.8
5	6.5	1.4053	Yes	35.4
6	7.6	1.6483	Yes	31.2
7	15.1	2.0225	Yes	21.4
8	30.2	2.2318	Yes	17.2

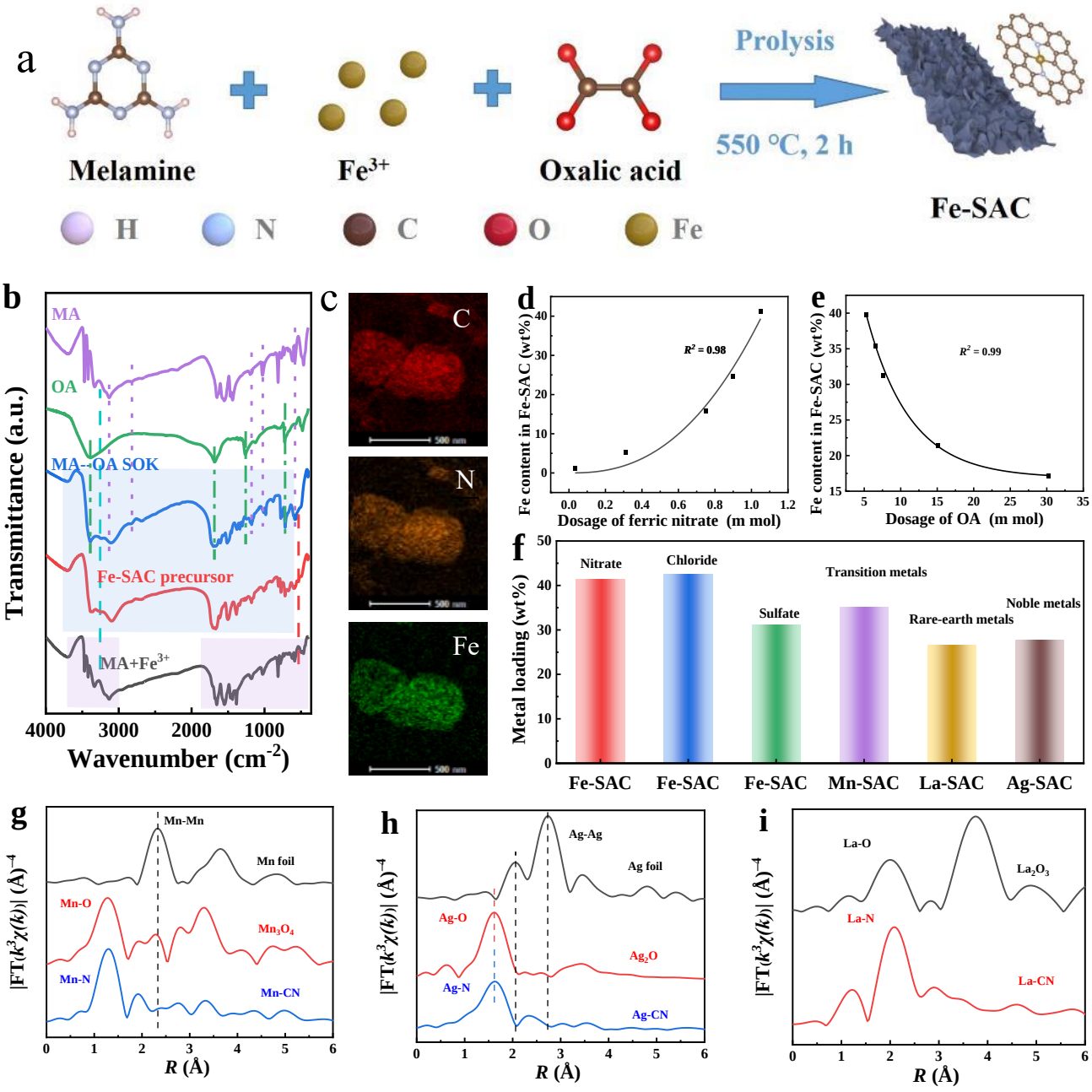

Fig. 2 | Schematic illustration of cascade anchoring strategy for controllable preparation of SACs with ultrahigh metal loadings. a, Schematic synthesis process for Fe-SAC-x catalyst with high Fe loading. b, Fourier transformed infrared (FTIR) spectra of catalyst precursors. c, Elemental mappings of Fe-SAC precursor obtained by the cascade anchoring strategy. d, Linear fitting relationship between SA wt% and metal

salt dosage. e, Linear fitting relationship between SA wt% and OA dosage. f, The metal loading of SAC prepared using different metal salts (nitrate, chloride or sulfate) and metal types (transition, rare-earth or noble metals). g-i, Fourier transform of K-edge EXAFS spectra of Mn-SAC, Ag-SAC and La-SAC, respectively.

Lines 671-705:

Notably, Fig. 4f reveals a positive correlation between k and the number of active sites. However, this positive correlation is non-linear, and the catalytic kinetics are significantly accelerated at high loadings. Assuming that each site exhibits similar intrinsic activity, the apparent rate constant k should theoretically display a linear or quasi-linear relationship with the total number of active sites. Combined with the electronic structure changes of Fe sites at high loadings, it collectively demonstrates the potential existence of long-range Fe-Fe interactions at elevated metal loadings, which enhances the catalytic activity of active sites. In addition, when the metal loading exceeds 24.62 wt%, the evolution of k values accelerates markedly, suggesting the existence of a critical loading threshold beyond which these long-range interactions become significantly enhanced.

To validate the above conclusions, we investigated the PMS catalytic performance at identical Fe active sites in catalyst models with varying metal loadings by DFT. It was observed that the PMS adsorption energy significantly increased when the metal loading reached 24.62 wt%, and as the loading continued to rise, the adsorption energy further changed (Fig. 4g). Additionally, the interaction between Fe sites and PMS exhibited enhanced differentiation due to intermetallic effects. Specifically, the electron

depletion region of the Fe adsorption center expanded markedly, while the bonded O atom accumulated more electrons. Bader charge analysis further revealed an increase in electron transfer from isolated Fe atoms to PMS molecules under higher Fe loading (Fig. 4g). This demonstrates that long-range metallic interactions at high loadings facilitate the activation of PMS by Fe site. This result is consistent with the open circuit potential test, indicating that catalysts with higher mass loading triggered higher potential jumps **(Fig.4a)**. Catalysts with higher metal loading simultaneously exhibited lower charge transfer resistance **(Fig. 3d)**, which collectively proves that elevated metal loading is beneficial for promoting the conductive bridging of Fe atoms to facilitate charge migration. Notably, when the metal loading surpassed the critical threshold of 24.62 wt%, the energy barriers of the $^1O_2$ generation pathway and rate-determining step (RDS) decreased substantially (Fig. 4h, $\Delta E_{rds,41.31} = 1.16$ eV $<$ $\Delta E_{rds,24.62} = 1.19$ eV $<$ $\Delta E_{rds,15.82} = 1.47$ eV $<$ $\Delta E_{rds,5.16} = 2.12$ eV). These theoretical analyses, combined with experimental results, including the OCP (Fig. 4a), i-t curves (Fig. 4b), and SMX degradation kinetics (Fig. 4f), collectively demonstrate that long-range Fe-Fe interactions are significantly enhanced beyond the critical loading threshold of 24.62 wt%. These interactions play a pivotal role in reducing energy barriers and improving electron transfer efficiency.

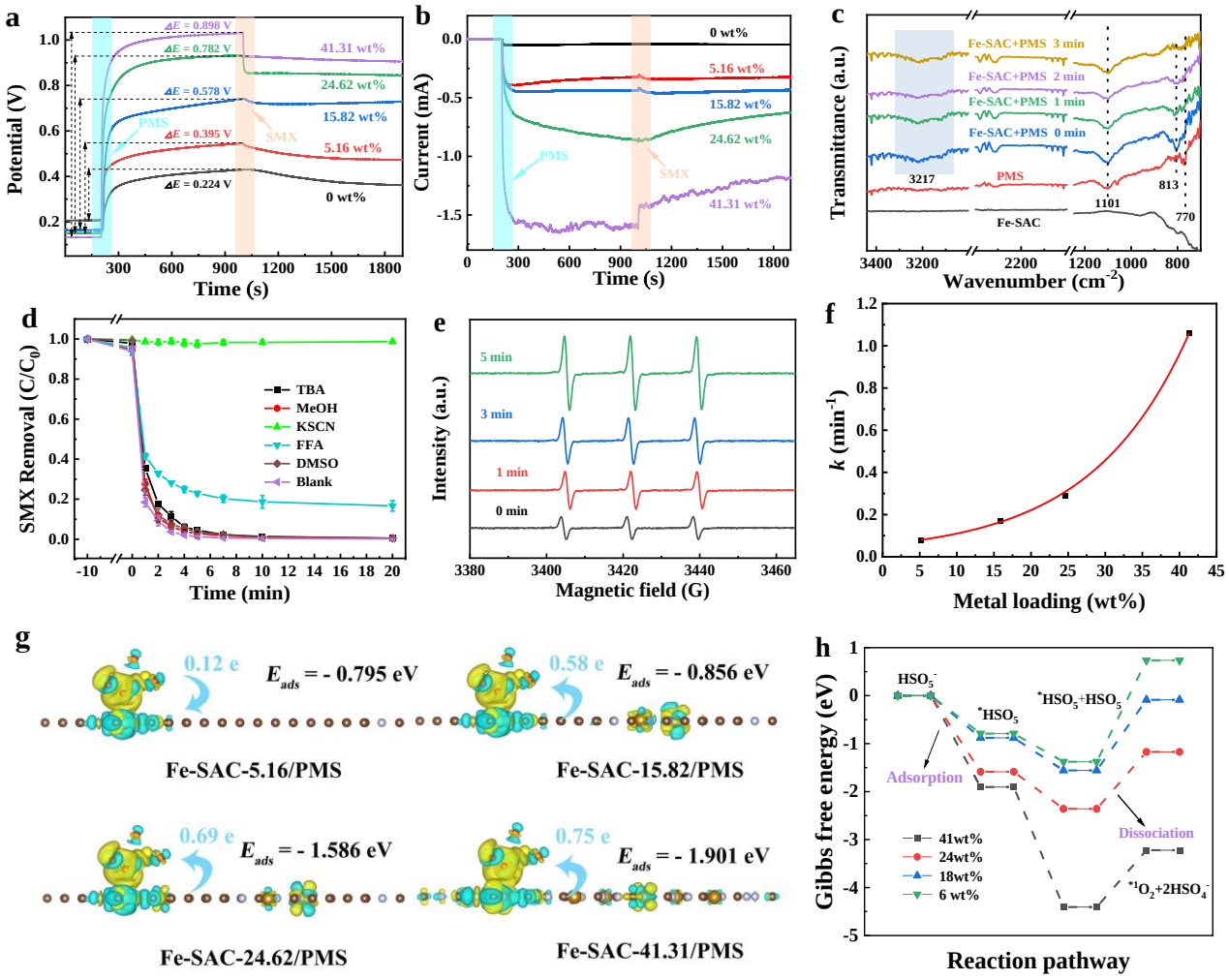

Fig. 4 | Evaluation of catalytic mechanism under gradient metal loading. a, The open-circuit potential changes of Fe-SAC-x when PMS or SMX is added respectively. b, Effects of PMS or SMX addition on the i-t curves at the corresponding open circuit potential. c, In situ FTIR spectra of Fe-SAC, PMS alone, and Fe-SAC combined with PMS. d, Effects of quenching reactive oxygen species on the degradation of SMX. e, Electron paramagnetic resonance spectra of TEMP-$^{1}O_2$ during SMX degradation in the Fe-SAC-4.31/PMS system. f, The relationship between metal loading and the apparent rate constant (k). g, Adsorption energy of PMS by Fe-SAC-x and the differential charge

density, bader charge transfer after the adsorption of PMS by Fe-SAC-x with different Fe loading. h, Energy profiles of $^1O_2$ derived reaction on varying Fe density models.

Comment 4. In Figure 1a and Figure 1b, the image ruler is not high-definition. Please correct it.

Response:

Thank you for bringing this to our attention. We have replaced the original images in Figures 1a and 1b with high-resolution versions to ensure optimal clarity. The updated figures now meet the journal's image quality standards.

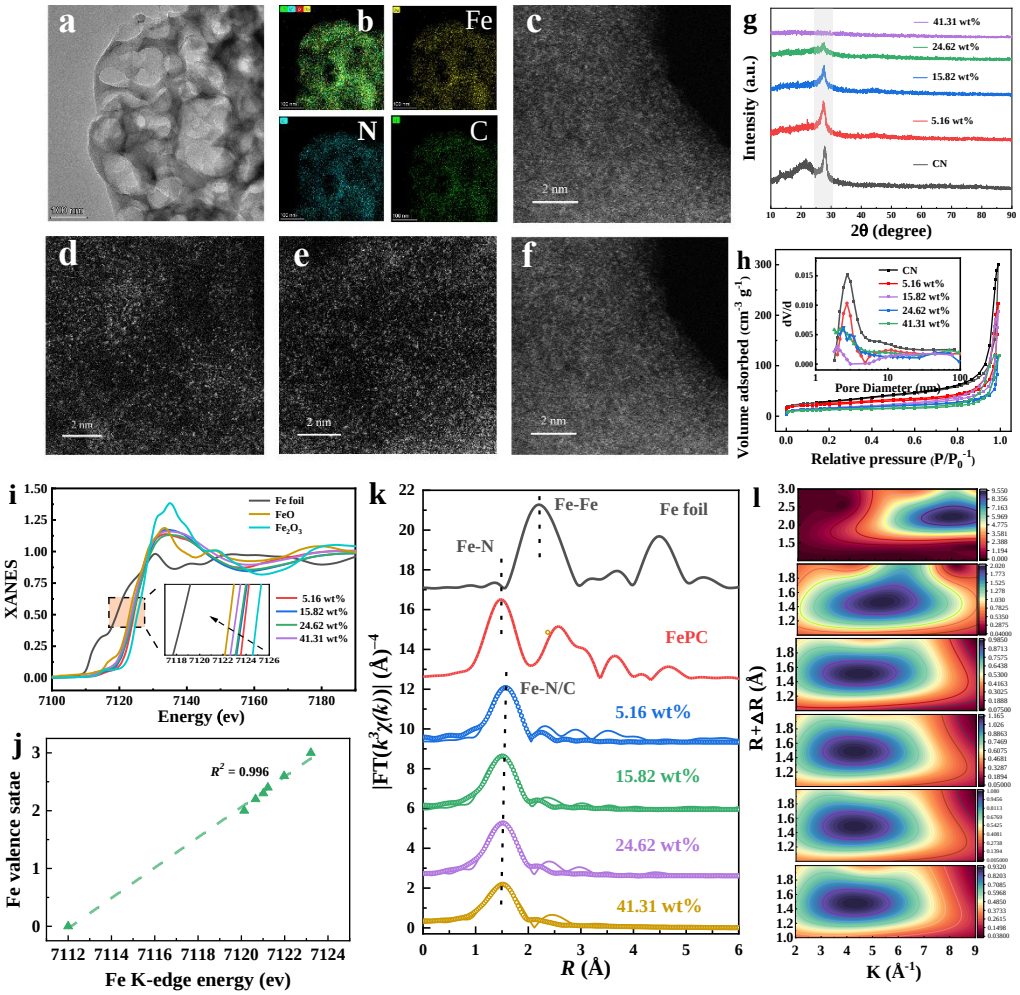

Fig. 1 | Structural characterizations of Fe-SAC-x. a-b, HRTEM and elemental mappings of Fe-SAC-41.31. c-f, HAADF-STEM images of Fe-SAC-x with metal loads was 41.31 wt%, 5.16 wt%, 15.82 wt% and 24.62 wt%, respectively. g, X-ray diffraction (XRD) patterns of as-prepared Fe-SAC-x. h, N_2 sorption isotherms and pore size distribution (inset) for iron-anchored catalysts with different iron loadings. i, Normalized XANES spectra of Fe-SAC-x samples. j, The oxidation state of iron decreased with the increase of metal loading. k, k^3-weighted Fourier transforms. l, wavelet transform of the experimental EXAFS spectra of the indicated catalysts.

Reviewer #3:

The manuscript presents a strategy for synthesizing high-loading single-atom catalysts (SACs) and their application in activating peroxymonosulfate (PMS) for the degradation of organic pollutants. While the work demonstrates potential application value, several critical issues must be addressed before it can be considered for publication. Below are the detailed concerns that warrant rejection of the manuscript:

Response to Reviewer #3

We deeply appreciate your rigorous evaluation and profound insights, which will fundamentally improve the scientific rigor of this work. Your nine pivotal comments have guided us to make systematic revisions, involving substantial experimental and theoretical enhancements. Below we provide detailed responses to each query, and the corresponding revisions have been incorporated into the manuscript.

Comment 1. The proposed cascade anchoring method for synthesizing high-loading SACs lacks sufficient novelty. Similar approaches have been extensively reported in the literature (e.g., Adv. Mater. 2024, 36, 2404900; Nat. Chem. 2021, 13(9): 887-894; Nat. Commun. 2019, 10(1), 1278). Notably, the study in Nat. Commun. 2019 employed glucose as an anchor and C_3N_4 as the substrate, yet achieved significantly lower metal loading compared to the 41.31 wt% reported in this manuscript. The authors fail to provide a convincing explanation for the exceptionally high loading achieved in their work, nor do they elucidate the underlying mechanisms ensuring the stability of these high-loading SACs.

Without a clear differentiation from existing methods and a robust mechanistic explanation, the novelty and scientific contribution of the synthesis strategy remain questionable.

Response:

We sincerely appreciate the reviewer's critical evaluation and guidance in conducting these seminal studies, which have enriched our perspective on SAC synthesis strategies. We fully acknowledge the importance of clearly differentiating our methodology from prior approaches and are pleased to elaborate on the unique innovations and mechanism foundations of our cascade anchoring strategy. Although these cited studies may appear superficially similar to our work at first glance, critical analysis reveals fundamental divergences in principles of methodology and mechanism. We respectfully maintain that these precedents will not diminish the novelty or originality of our synthetic strategy. Below, we will address the novelty concerns through three key aspects: (I) Critical distinctions from cited work, (II) The mechanism of stabilizing high-load Fe-SAC in the C_3N_4 substrate, and (III) Quantitative evidence to explain ultrahigh loading capability.

(I) Critical distinctions from cited work

(a) As is well known, achieving high-density single-atom catalysts (SACs) has long been a critical challenge in SAC development, and there remains a lack of simple and universal synthesis strategies. Consequently, numerous researchers have been dedicated to exploring methods for enhancing SAC loading capacity, with some

progress achieved. As recommended by the reviewer (Adv. Mater. 2024, 36, 2404900), the cited study employed direct pyrolysis of thiourea-copper ion complexes to increase the Cu loading on carbon nitride (Cu/CN). Although the maximum loading reached only 9.97 wt%, the XRD patterns of Cu/CN-x samples (Figures S9 and S15) in that work exhibit distinct C_3N_4 diffraction peaks, indicating well-preserved periodic triazine units (rich in nitrogen) in the substrate. This suggests that substantial N-coordination sites remained unutilized, which partially explains why their metal loading is significantly lower than that in our study (41.31 wt%). Furthermore, their synthetic strategy shows limitations. Although the loading of Cu/NC systems reached 9.97 wt%, the loading of other metal systems was merely ~0.5 wt% (Figure S49). This specificity originates from the unique complexation-polymerization capability between thiourea and Cu^{2+} ions, which cannot be effectively applicable to other metal ions. In contrast, melamine molecules inherently contain much higher nitrogen content than thiourea, providing a more abundant coordination environment for metal ions. This fundamental distinction constitutes one of the key reasons why our synthesis strategy can achieve ultrahigh metal loading.

(b) In Nat. Chem. 2021, 13(9), 887-894, the authors first synthesized amine-functionalized graphene quantum dots (GQDs) and utilized the coordination between surface amine groups and metal cations to adsorb metals onto the GQD surface. Subsequently, GQDs loaded with metal were physically mixed with urea and pyrolyzed to prepare high-loading Ir-SACs. This strategy differs fundamentally from our approach in several aspects. Firstly, their ability to achieve high metal loading relies

critically on the small particle size and high surface-to-volume ratio of GQDs. When applied to other carbon materials (e.g., nitrogen-doped graphene reported in their work), amine functionalization fails to provide high Ir-SAC loading. Notably, the synthesis of GQDs requires high-temperature hydrothermal treatment and prolonged dialysis, with extremely low yields, which inherently limits the scalability of their method. Secondly , to provide sufficient coordination elements for metal ions, they employed physical mixing of metal-chelated GQD powders with urea, rather than the self-assembly of metal-oxalate complexes with melamine emphasized in our work (implementing bottom-up molecular level control). Finally, although their study achieved an impressive Ir mass loading (41.6 wt%, comparable to our Fe loading of 41.31 wt%), the relative atomic mass of Ir (192 g mol^{-1}) is 3.4 times that of Fe (55.8 g mol^{-1}). This implies that our Fe-SACs exhibit a significantly higher density of metal active sites. Furthermore, when extending their strategy to Ni-SACs (with a relative atomic mass similar to Fe), only a mass loading of 15.4 wt% was obtained, further highlighting the superiority of our synthetic strategy.

(c) In Nat. Commun. 2019, 10(1), 1278, the synthetic strategy differs substantially from our work. Although melamine was used as a nitrogen source, the actual substrate in their study is porous carbon rather than C_3N_4, as the high pyrolysis temperature (800℃) inevitably causes the decomposition of C_3N_4. This is fundamentally different from our approach. Furthermore, the authors physically ground the metal-chelated porous carbon with melamine, which is similar to that in Nat. Chem. 2021, 13(9), 887-894, rather than employing the molecular/atomic-level control emphasized in our work

(i.e., self-assembly of metal-oxalate complexes with melamine molecules). Due to inhomogeneous dispersion, their approach leads to inevitable waste of N-coordination species, which partially explains why their Fe loading is much lower than that achieved in our study. Additionally, their strategy involves anchoring metal atoms onto a pre-synthesized support (porous carbon), while our method adopts a bottom-up in situ self-assembly and self-growth strategy. These intrinsic differences result in lower metal loading compared to our results.

Although the aforementioned synthesis strategies all utilize coordination chemistry (which might superficially suggest similarity to our work), coordination alone cannot fully account for the ultrahigh metal loading achieved in our study. Our innovations lie in:

- Coordination complexation between oxalic acid and metal ions;
- Composite reaction between metal-chelated oxalate complexes and melamine enables metal ions to be synchronously assembled into a supermolecular organic framework;
- In situ decomposition of oxalic acid during pyrolysis;
- Full utilization of abundant pre-anchored N-coordination sites by metal ions during thermal treatment.

Our synthesis strategy can be analogized to hemoglobin transporting oxygen:

- Hemoglobin (analogous to oxalic acid) acts as a specific carrier that binds and delivers oxygen (metal ions) to biological cells (melamine).
- Hemoglobin subsequently dissociates (corresponding to the decomposition of

oxalic acid during pyrolysis), ensuring that each "cell" (melamine monomer in the supermolecular framework) pairs with its own "oxygen" (metal ion).

This process guarantees atomic-level uniformity of metal dispersion in the framework and maximizes the utilization of N-coordination species during subsequent pyrolysis.

This mechanism fundamentally differs from those in Adv. Mater. 2024, 36, 2404900; Nat. Chem. 2021, 13(9), 887-894; and Nat. Commun. 2019, 10(1), 1278, where coordination chemistry alone fails to achieve such precision or efficiency.

(II) The mechanism of stabilizing high-load Fe-SAC in the C_3N_4 substrate

To ensure the stability of high-loading SACs, two critical conditions must be met : First of all, the carrier must provide sufficient coordination atoms to stabilize a large number of metal atoms. C_3N_4 with periodic triazine structures and high nitrogen content is undeniably one of the most optimal substrates for preparing high-loading SACs. Secondly, full utilization of coordination sites on the substrate is essential. This requires innovative synthesis strategies that can achieve molecular or atomic-level control. A key approach involves the atomically uniform dispersion of metal atoms in the catalyst precursor, followed by pyrolysis to utilize nearby N-coordination species in situ during thermal treatment. Compared with conventional methods, these principles underpin the superior stability and loading capacity of our SAC.

To provide compelling experimental evidence, we systematically tracked the bottom-up self-assembly process of the SAC precursor (supramolecular organic framework before pyrolysis step). Supplementary Fig. 3a demonstrates the composite

reaction between melamine (MA) and oxalic acid (OA), yielding a milky-white supramolecular organic framework. Fourier transform infrared (FTIR) spectroscopy (Fig. 2b) revealed that the characteristic peaks of MA (580.8, 1025.2, 3133.7 cm^{-1}) or OA (713.5, 1686.9, 3388.7 cm^{-1}) disappeared in the supramolecular framework system, while a new amide peak emerged at 3254.5 cm^{-1}, confirming chemical assembly rather than physical mixing between MA and OA. Upon introducing Fe^{3+}, the resulting supramolecular polymer exhibited a homogeneous yellow-green color (Supplementary Fig. 3b) with a clarified solution, indicating that OA not only chelates Fe^{3+} but also co-assembles with MA, thereby synchronously anchoring Fe^{3+} into the organic framework.

FTIR analysis further verified the chemical anchoring of Fe^{3+}. The appearance of a Fe-O bonding peak at 533 cm^{-1} (Fig. 2b) confirmed the successful integration of Fe atoms into the skeleton via chemical bonding. The spectrum of Fe-SAC precursor perfectly matched that of supramolecular polymer framework, demonstrating that the chelation of $Fe^{3+}$with OA did not disrupt the skeleton structure. In stark contrast, the precursor prepared by the solvent evaporation method (Supplementary Fig. 3c) displayed a spectrum nearly identical to that of pure MA, with no detectable Fe-O bonding peaks (Fig. 2b), confirming only physical adsorption of Fe^{3+} onto MA.

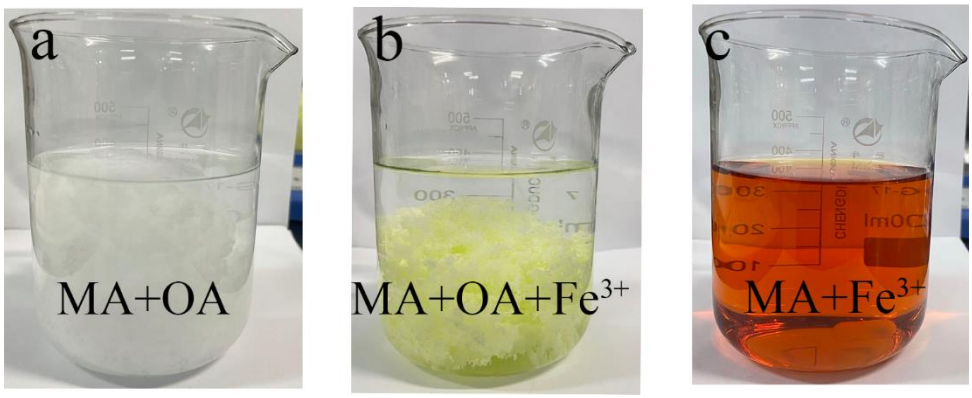

Supplementary Fig. 3 | a, Supramolecular organic skeleton generated by the complexation reaction between MA and OA; b, SAC precursor after anchoring Fe^{3+}; c, SAC precursor prepared by conventional steam-drying solvent method.

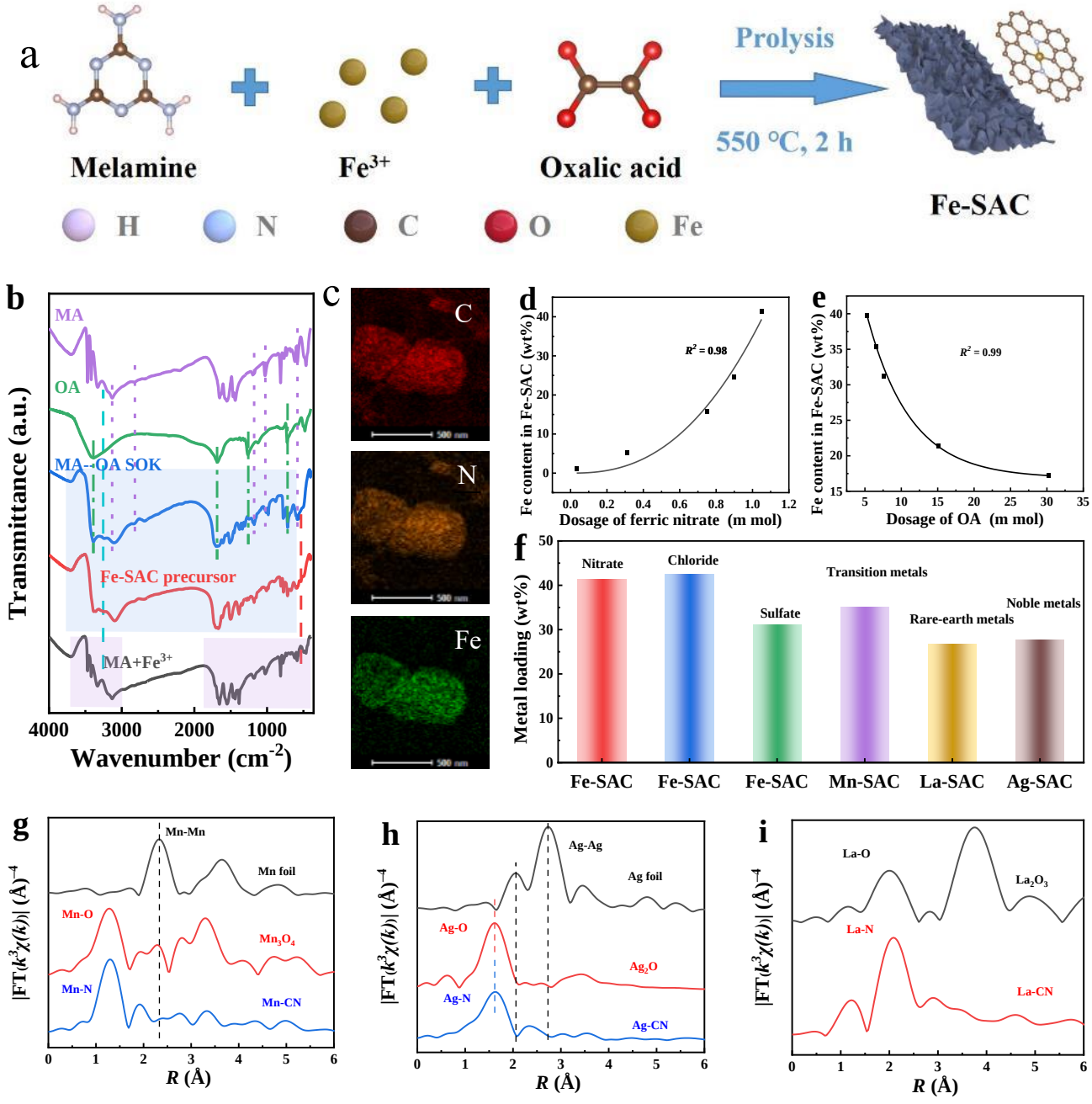

Fig. 2 | Schematic illustration of cascade anchoring strategy for controllable preparation of SACs with ultrahigh metal loadings. a, Schematic synthesis process for Fe-SAC-x catalyst with high Fe loading. b, Fourier transformed infrared (FTIR) spectra

of catalyst precursors. c, Elemental mappings of Fe-SAC precursor obtained by the cascade anchoring strategy. d, Linear fitting relationship between SA wt% and metal salt dosage. e, Linear fitting relationship between SA wt% and OA dosage. f, The metal loading of SAC prepared using different metal salts (nitrate, chloride or sulfate) and metal types (transition, rare-earth or noble metals). g-i, Fourier transform of K-edge EXAFS spectra of Mn-SAC, Ag-SAC and La-SAC, respectively.

To validate the proposed mechanism, we further investigated the morphology of Fe-SAC precursor (Fe^{3+}-anchored organic framework) via TEM characterization. The Fe-SAC precursor prepared by conventional solvent evaporation method exhibited a fine rod-like structure (Supplementary Fig. 4a), accompanied by unevenly distributed metal particles. This observation confirms the physical combination and non-uniform metal distribution on the precursor, which inevitably leads to insufficient utilization of coordination species on the carrier. Such heterogeneity necessitates post-synthesis treatments (e.g., acid washing or multistep annealing) to remove unbound metal species, ultimately resulting in low catalyst loading [10].

In stark contrast, the Fe-SAC-41.31 precursor synthesized via our cascade anchoring strategy displayed an irregular morphology without particle aggregation (Supplementary Fig. 4b). EDX mapping further confirmed the homogeneous distribution of Fe elements across the framework (Fig. 2c). This sharp contrast conclusively demonstrates the critical role of oxalic acid as a specific carrier that enables targeted delivery of Fe^{3+} into the supramolecular organic framework. This mechanism ensures the full utilization of coordination species on the precursor during

subsequent pyrolysis, directly contributing to the ultrahigh metal loading achieved in our work.

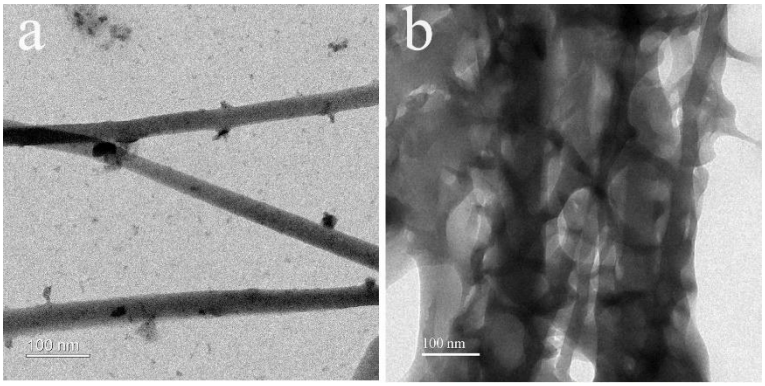

Supplementary Fig. 4 | TEM images of Fe-SAC precursor obtained by a, conventional solvent evaporation method; b, cascade anchoring strategy.

These results unequivocally validate that our self-assembly strategy ensures atomic-level dispersion and chemical stabilization of metal ions within the supramolecular framework, which is a critical prerequisite for the in-situ utilization of nearby N-coordinating species by Fe atom in the subsequent pyrolysis process to achieve ultrahigh metal loading in SACs.

(III) Quantitative evidence to explain ultrahigh loading capability

The synthesis process of SAC through pyrolysis of supramolecular organic frameworks was monitored by thermogravimetric analysis (TGA) (Supplementary Fig. 5). The initial mass attenuation below 110℃ is attributed to the volatilization of residual moisture in the sample. A pronounced mass attenuation observed in the MA sample between 250-350℃ corresponds to its thermal polycondensation into C_3N_4. In contrast, the MA-OA composite supramolecular framework exhibited significant mass

attenuation at lower temperatures due to the thermal decomposition of thermally labile oxalic acid. Notably, the direct pyrolysis of MA without oxalic acid yielded C_3N_4 with a densely packed bulk structure (Supplementary Fig. 6a), with a specific surface area of merely 18.74 m^2 g^{-1} (Supplementary Table 2). The pyrolysis of the supramolecular framework produced C_3N_4 with a petal-like flaky architecture (Supplementary Fig. 6b), exhibiting an enhanced specific surface area of 100.05 m^2 g^{-1}. This structural modification is ascribed to the liberation of CO_2 from the decomposed oxalate species during calcination, which disrupts the polycondensation of melamine and facilitates the formation of porous structures conducive to reactant diffusion in the catalytic processes. Remarkably, the Fe-SAC precursor anchored with Fe^{3+} ions displayed accelerated mass attenuation at reduced temperatures (Supplementary Fig. 5), indicating the catalytic role of Fe species in promoting the volatilization of thermally unstable components.

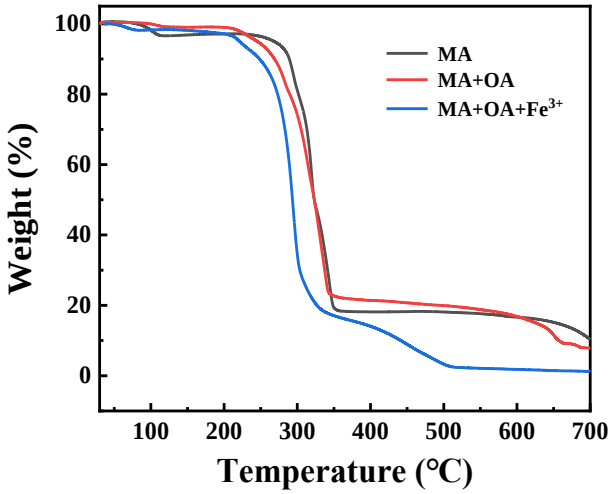

Supplementary Fig. 5 | Thermogravimetric curves of MA, MA+OA supramolecular organic skeleton and Fe-SAC precursor, respectively.

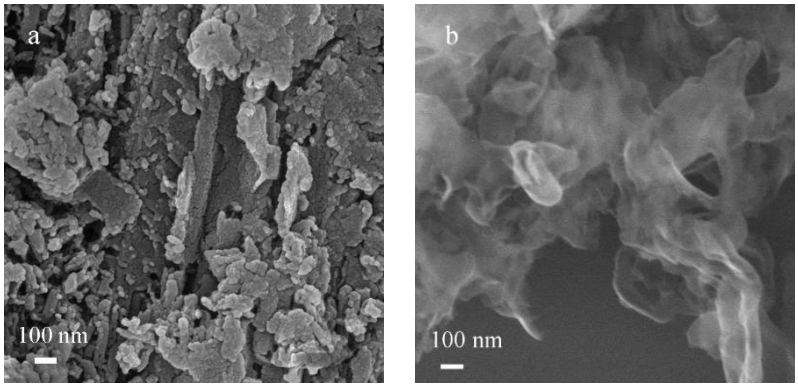

Supplementary Fig. 6 | SEM images of C_3N_4 prepared by pyrolysis of MA (a) or MA+OA supramolecular polymers (b).

Supplementary Table 2 | BET surface area, pore diameter and mesoporous pore volume of as-prepared catalysts.

Sample	BET surface (m^2/g)	Pore diameter (nm)	Mesoporous pore volume (cm^3/g)
C_3N_4(MA)	18.74	18.55	0.122
CN(MA-OA)	100.05	21.89	0.464
Fe-SAC 5.16 wt%	84.06	27.29	0.344
Fe-SAC 15.82 wt%	57.55	25.36	0.321
Fe-SAC 24.62 wt%	55.44	20.91	0.181
Fe-SAC 41.31 wt%	46.10	24.06	0.176

To investigate the relationship between sintering temperature and the structure of SACs, the structural characteristics of the catalysts prepared at different pyrolysis temperatures (450, 550, 650℃) were characterized. As shown in Supplementary Fig. 8a, XRD analysis proved that no diffraction peaks of the metal phase were observed for

the catalyst prepared at 450℃, and no metal particle aggregates were observed by HRTEM (Supplementary Fig. 8b), indicating the formation of Fe-SACs during calcination at 450℃. However, the XRD patterns exhibit distinct C_3N_4 diffraction peaks, indicating well-preserved periodic triazine units in the substrate. This suggests that substantial N-coordination sites remained unutilized. Therefore, the incomplete decomposition of unstable components in the substrate resulted in a relatively low metal proportion, with a loading of 15.3 wt% (Supplementary Table 1). In contrast, calcination at 550℃ produced Fe-SACs with a high metal loading of 41.31 wt%. Further increasing the temperature to 650℃ led to the emergence of distinct lattice diffraction peaks in the XRD patterns (Supplementary Fig. 8a), indicating intensified thermal motion of metal atoms at elevated temperatures and subsequent formation of crystalline structures (Supplementary Fig. 8d). Therefore, 550℃ is identified as the optimal synthesis temperature for preparing high-loading single-atom catalysts.

Supplementary Table 1 | Relationship between metal salts content, SAC precursor yield, and metal loading of as prepared SAC.

Sample	Metal salts (mmol)	SAC precursor yield (g)	Metal contents (wt%)
Fe-SAC-5.16	0.3	1.74	5.16
Fe-SAC-15.82	0.75	1.67	15.82
Fe-SAC-24.62	0.9	1.62	24.62
Fe-SAC-41.31	1	1.53	41.31
Fe-SAC (450℃)	1	1.55	15.31
Mn-SAC	1	1.55	35.13
Ag-SAC	1	1.51	27.04

La-SAC	1	1.76	22.62
CN	0	3.78	0
Fe-SAC-T	1	3.53	1.61

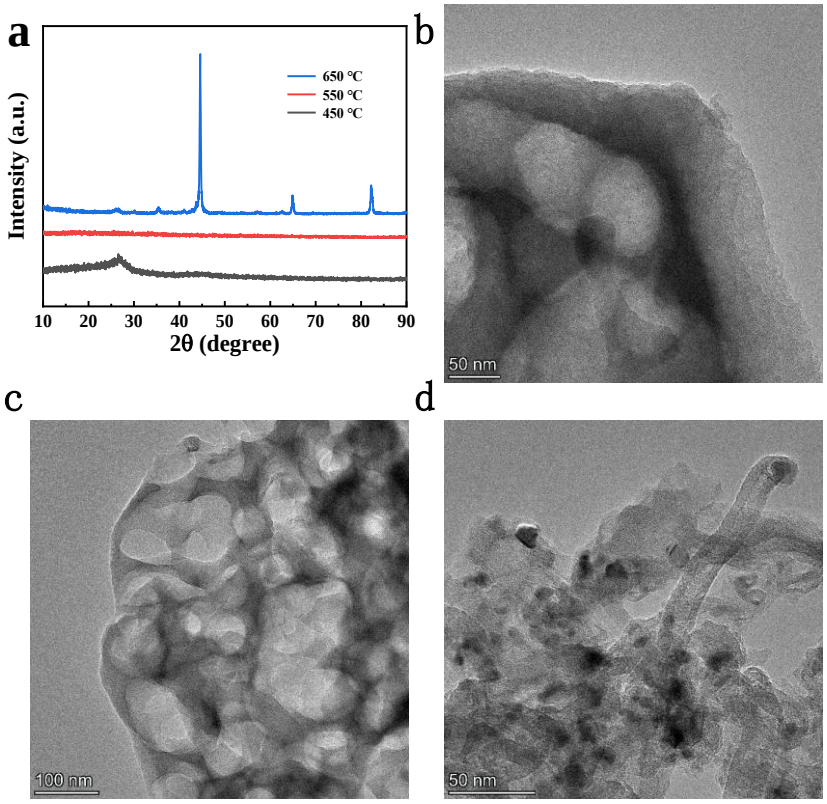

Supplementary Fig. 8 | a, XRD patterns of catalysts calcined at different temperatures. b-d, HRTEM images of catalysts calcined at 450, 550 and 650℃, respectively.

The final high loading Fe-SAC was obtained through pyrolysis of the precursor. The morphology of the SAC samples was observed by high-resolution transmission electron microscopy (HRTEM), the obtained Fe-SAC inherited the stacked-layered features of C_3N_4 with a rich porous structure (Fig. 1a). The elemental mapping showed that Fe, N, C and O species were uniformly distributed in density on the substrate (Fig. 1b), suggesting that iron element may be anchored to the carbon substrate in an

atomically dispersed form. The high angle annular dark field scanning transmission electron microscopy (HAADF-STEM, Figs. 1c-f) further revealed the dispersion imaging of Fe atoms, manifested as isolated bright spots densely distributed on the carbon substrate, which is due to the much higher electron density of Fe than that of nonmetals, proving that high-mass-loaded Fe exists in the form of single atoms.

The X-ray diffraction spectra of all Fe-SACs samples did not reveal features associated with iron metals or iron oxides, only showing the reflection of the carrier material (Fig. 1g). In pristine CN, two typical diffraction peaks at 21.4◦ and 27.8◦ corresponded to the repetitive heptazine structural units and interlayer stacking in carbon nitride[11]. It is worth noting that the signal intensities decreased and eventually disappeared with the increase of metal loading of pyrolyzed catalyst, suggesting that the highly loaded monatomic metals disrupted the native structure of CN. This phenomenon arises from the coordination of abundant Fe atoms with nitrogen atoms in the substrate at elevated temperatures, forming stable Fe-Nx configurations that disrupt the periodic triazine units within the CN framework. This observation aligns with the TGA results, where the presence of iron species significantly accelerated the decomposition of thermally labile components in the precursor.

The chemical configurations and local coordination environments of Fe-SAC-x were investigated by the X-ray absorption spectroscopy (XAS). It can be seen from the X-ray absorption fine structure spectroscopy (XANES) curves of Fe K-edge that the near-edge energy adsorption thresholds of all Fe-SAC-x are higher than that of FeO but lower than that of Fe_2O_3 (Fig. 1i), suggesting that the valence states of Fe atoms in Fe-

SAC-x lie between +2 and +3[12]. Notably, the increase in the density of Fe sites promotes the shift of the absorption edge towards lower energy, suggesting that the electron density of Fe sites in high-loading Fe-SAC is higher than that in low-loading Fe-SAC[13]. The valence states of catalyst with different metal loading were fitted (Fig. 1j), and it was found that the valence states of Fe were 2.6, 2.4, 2.3, 2.2 in sequence as the iron loading increased. Therefore, elevating the Fe loading in Fe-SACs is beneficial to regulate the local electron density of Fe single atoms. The Fourier transform (FT) k^3-weighted EXAFS spectra (Fig. 1k) show that the extended-edge X-ray absorption fine spectra of all Fe-SACs display a main peak near 1.5 Å, corresponding to the Fe-N/C bond, suggesting the presence of isolated Fe-based species in all samples. In addition, no metal-metal distance feature between 2.1 and 2.5 Å was observed in any samples, confirming the absence of metal nanoparticles or clusters[14]. The wavelet transform (WT) further provides radial distance resolution as well as K-space analysis, and the Fe-SACs show a maximum peak at ~4.4 $Å^{-1}$ (Fig. 1l), which is consistent with the EXAFS results in R-space. These results consistently support that Fe in Fe-SAC with different Fe loading is atomically dispersed. It is noteworthy that a decrease in k value is observed on the WT isograms of all Fe-SAC-x samples compared to FePc, which is attributed to the introduction of C in the first coordination shell layer of Fe atoms[15], suggesting that in addition to N atoms, Fe atoms also coordinate with C atoms. In addition, the exact coordination structure of Fe atoms was determined by quantitative least-squares EXAFS fitting (Supplementary Table 3), supporting that the coordination environment of Fe in Fe-SAC-x is similar to that of FePc, and the coordination number of the first

coordination layer of Fe in Fe-SAC is 4.1 ± 0.4.

Supplementary Table 3 | EXAFS fitting parameters for various Fe-SAC-x samples.

Sample	Shell	N^a	$R(Å)^b$	$\sigma^2(Å^2)^c$	$\Delta E_0(eV)^d$	*R* factor
FePC	Fe-N	4	1.96	0.0068	1.9	0.0124
Fe-SAC-5.16	Fe-N	3.7	2.09	0.0132	4.91	0.0226
Fe-SAC-15.82	Fe-N	4.4	2.04	0.0171	3.4	0.0188
Fe-SAC-24.62	Fe-N	4.2	2.04	0.0195	5.15	0.0199
Fe-SAC-41.31	Fe-N	4.1	2.04	0.0196	4.44	0.0151

N^a: coordination numbers; $R(Å)^b$: bond distance; $\sigma^2(Å^2)^c$: Debye-Waller factors; $\Delta E_0(eV)^d$: the inner potential correction. *R* factor: goodness of fit. S_0^2 was set to 0.848, according to the experimental EXAFS fit of Fe foil by fixing CN as the known crystallographic value.

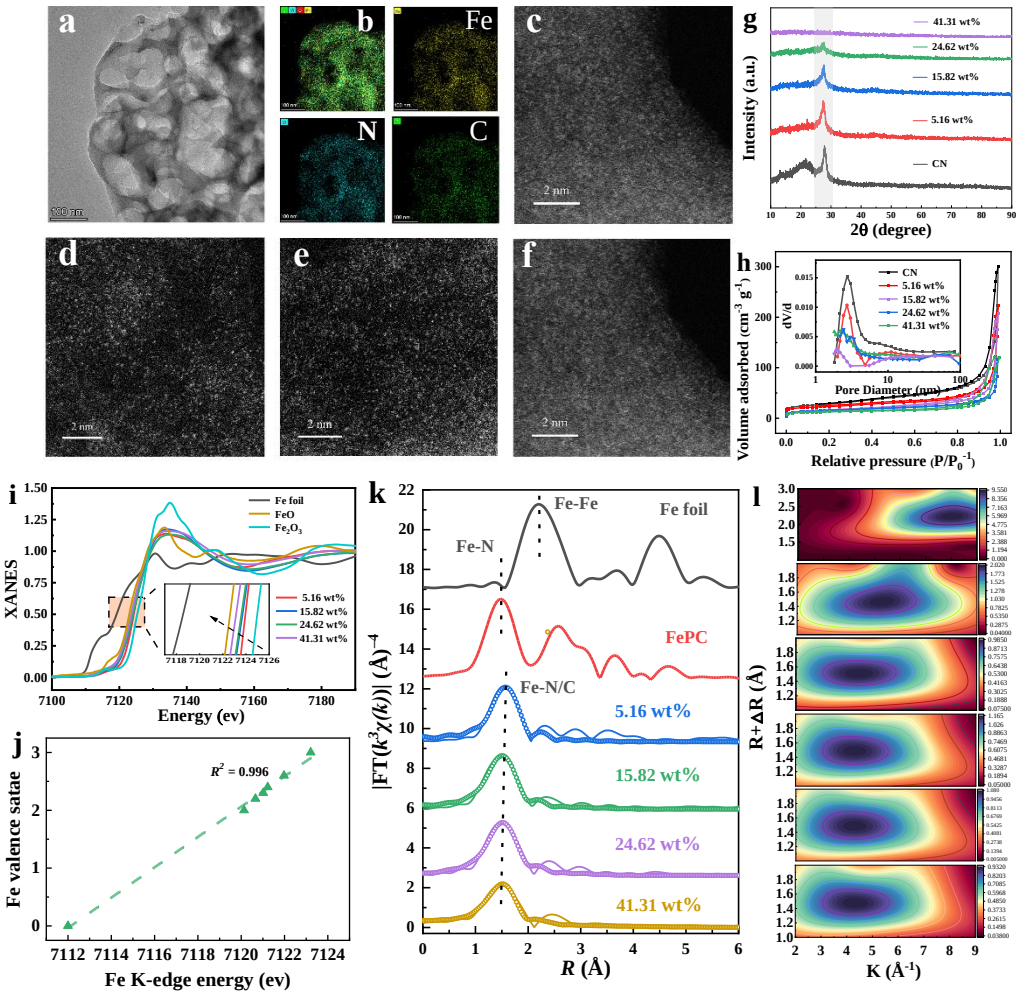

Fig. 1 | Structural characterizations of Fe-SAC-x. a-b, HRTEM and elemental mappings of Fe-SAC-41.31. c-f, HAADF-STEM images of Fe-SAC-x with metal loads was 41.31 wt%, 5.16 wt%, 15.82 wt% and 24.62 wt%, respectively. g, X-ray diffraction (XRD) patterns of as-prepared Fe-SAC-x. h, N_2 sorption isotherms and pore size distribution (inset) for iron-anchored catalysts with different iron loadings. i, Normalized XANES spectra of Fe-SAC-x samples. j, The oxidation state of iron decreased with the increase of metal loading. k, k^3-weighted Fourier transforms. l, wavelet transform of the experimental EXAFS spectra of the indicated catalysts.

Concluding Statement:

We sincerely thank the reviewer for raising critical questions about the novelty and mechanistic underpinnings of our work. Through this detailed response, we have demonstrated that our cascade anchoring strategy fundamentally differs from previous SAC synthesis methods in terms of design philosophy and execution.

What's the difference?

The precise molecular-level control in this study differs from the physical mixing in cited works. Unlike prior methods relying on physical mixing or post-synthesis anchoring (e.g., Nat. Commun. 2019), our OA-mediated self-assembly ensures atomic dispersion of metal ions (Fe^{3+}) within the MA-OA framework before pyrolysis. This "pre-anchoring" guarantees the full utilization of N-coordination sites during thermal treatment (validated by FTIR, TEM/EDX; Figs. 2b–c, Supplementary. Figs. 3–4).

Why higher loading and stable?

Pre-anchoring combined with in situ N-site utilization. Bottom-up cascade anchoring strategy anchors Fe metal atomically to the synchronously generated supramolecular organic backbone. During the pyrolysis, the decomposition of OA (TGA, Supplementary Fig. 5) liberates CO_2 to create porous C_3N_4 (BET: 100.05 m^2/g^{-1} vs. 18.74 m^2 g^{-1} for bulk C_3N_4; Supplementary Fig. 6/Table 2), and Fe^{3+} coordinates with exposed N-sites simultaneously. This avoids N-site waste observed in conventional methods (e.g., Adv. Mater. 2024, thiourea-derived C_3N_4 with unused N-sites).

The abundant nitrogen-coordinating moieties to facilitate the formation of Fe-N_3C coordination, as well as the dynamic electronic modulation (Fe valence ↓) jointly promoted the stability of Fe sites. XANES/EXAFS (Figs. 1i–k) reveal that higher Fe loading lowers the oxidation state of Fe (2.6 → 2.2), thereby enhancing electron density and stabilizing Fe-N_3C configurations (EXAFS fitting, Supplementary Table 3). This electronic adaptability prevents aggregation even at 41.31 wt% (no Fe-Fe peaks in FT-EXAFS; Fig. 1k).

Our work not only resolves the long-standing challenge of balancing ultrahigh metal loading with atomic dispersion but also establishes a generalizable paradigm for SAC synthesis. We hope this clarification reaffirms the originality and significance of our methodology. We welcome further discussion to address any remaining concerns and will gladly incorporate additional analyses if requested.

Textual Revisions:

Lines 238-261:

During the preparation of Fe-SAC precursor, the metal ions are strongly assembled

into the supramolecular organic skeleton (SOK) through chemical bonding, and the subsequent high-temperature pyrolysis further anchors the metal atoms in-situ at the nearby N sites. Fig. 2a illustrates this simple synthesis strategy. Fe^{3+} was assembled into the SOK of oxalate-melamine macromolecules using OA because it can either chelate with Fe^{3+} [Eq. (1)] or react with melamine (MA) to form a supramolecular organic framework [Eq. (2)]. Supplementary Fig. 3a further demonstrates the composite reaction between MA and OA, yielding a milky-white supramolecular organic framework. Fourier transform infrared (FTIR) spectroscopy (Fig. 2b) revealed that the characteristic peaks of MA (580.8, 1025.2, 3133.7 cm^{-1}) or OA (713.5, 1686.9, 3388.7 cm^{-1}) disappeared in the supramolecular framework, while a new amide peak emerged at 3254.5 cm^{-1}, confirming chemical assembly rather than physical mixing between MA and OA. Upon introducing Fe^{3+}, the resulting supramolecular polymer exhibited a homogeneous yellow-green color (Supplementary Fig. 3b) with a clarified solution, indicating that OA not only chelates Fe^{3+} but also co-assembles with MA, thereby synchronously anchoring Fe^{3+} into the organic framework. In the FTIR profile, the appearance of a Fe-O bonding peak at 533 cm^{-1} (Fig. 2b) confirmed successful integration of Fe atoms into the skeleton via chemical bonds. The spectrum of the Fe-SAC precursor perfectly matched that of the supramolecular polymer framework, demonstrating that the chelation of Fe^{3+} with OA did not disrupt the skeleton structure. In stark contrast, the precursor prepared by the solvent evaporation method (Supplementary Fig. 3c) displayed a spectrum nearly identical to that of pure MA, with no detectable Fe-O bonding peaks (Fig. 2b), confirming only physical adsorption of

Fe^{3+} onto MA.

Lines 272-346:

In stark contrast, the Fe-SAC-41.31 precursor synthesized via our cascade anchoring strategy displayed an irregular morphology without particle aggregation (Supplementary Fig. 4b). EDX mapping further confirmed the homogeneous distribution of Fe elements across the framework (Fig. 2c). This sharp contrast conclusively demonstrates the critical role of oxalic acid as a specific carrier that enables targeted delivery of Fe^{3+} into the supramolecular organic framework. This mechanism ensures the full utilization of coordination species on the precursor during subsequent pyrolysis, directly contributing to the ultrahigh metal loading achieved in our work.

The synthesis process of SAC through pyrolysis of supramolecular organic frameworks was monitored by thermogravimetric analysis (TGA) (Supplementary Fig. 5). The initial mass attenuation below 110°C is attributed to the volatilization of residual moisture in the sample. A pronounced mass attenuation observed in the MA sample between 250-350°C corresponds to its thermal polycondensation into C_3N_4. In contrast, the MA-OA composite supramolecular framework exhibited significant mass attenuation at lower temperatures due to the thermal decomposition of thermally labile oxalic acid. Notably, the direct pyrolysis of MA without oxalic acid yielded C_3N_4 with a densely packed bulk structure (Supplementary Fig. 6a), demonstrating a specific surface area of merely 18.74 m^2 g^{-1} (Supplementary Table 2). The pyrolysis of the supramolecular framework produced C_3N_4 with a petal-like flaky architecture

(Supplementary Fig. 6b), exhibiting an enhanced specific surface area of 100.05 $m^2 g^{-1}$. This structural modification is ascribed to the liberation of CO_2 from the decomposed oxalate species during calcination, which disrupts the polycondensation of melamine and facilitates the formation of porous structures conducive to reactant diffusion in the catalytic processes. Remarkably, the Fe-SAC precursor anchored with Fe^{3+} ions displayed accelerated mass attenuation at reduced temperatures (Supplementary Fig. 5), indicating the catalytic role of Fe species in promoting the volatilization of thermally unstable components. Notably, the presence of metal components also impacts the porosity and surface area of the catalyst. As shown in Fig. 1h, at fixed concentrations of OA and MA, the specific surface area of the catalyst decreased with increasing metal loading. This trend arises because metal species catalyze the decomposition of unstable components and competitively scavenge nitrogen atoms from MA during pyrolysis, thereby hindering the polycondensation of the supramolecular polymer into ordered C_3N_4. This effect intensifies at higher metal loadings, as evidenced by the gradual disappearance of characteristic heptazine unit diffraction peaks in the XRD patterns (Fig. 1g).

Intriguingly, for the final synthesized SAC, its Fe mass fraction does not increase linearly with the amount of Fe salt in the precursor (Fig. 2d), but exhibits an exponential growth trend. This indicates that a smaller incremental increase in Fe salt injection in the later stages can cause a significant rise in Fe loading. To elucidate this anomalous behavior, we systematically investigated the synthesis process of high-loading Fe-SACs. Given the critical role of OA in coordinating metal ions, the amount of OA added

was adjusted while maintaining a fixed concentration of MA and Fe salt. It was found that the OA content significantly influences both the yield of the Fe-SAC precursor and the ultimate metal loading of the SAC (Supplementary Table 4). This demonstrates a concentration-dependent relationship between MA, OA, and Fe^{3+}, and reveals that the supramolecular organic framework possesses a maximum metal loading capacity. Increasing the OA content generates more catalyst substrate (Supplementary Table 4), resulting in a corresponding reduction in metal loading (Fig. 2e). This counterintuitive phenomenon is the inverse of the trend observed in Fig. 2d, where increasing the Fe salt dosage while keeping MA and OA fixed gradually approaches the maximum loading capacity of framework, resulting in a rapid surge in metal loading. This systematic investigation reveals that oxalate acts as a "structure-directing agent" that governs framework integrity and metal stabilization capacity, rather than just a sacrificial template. The dosage of Fe^{3+} salt directly controls the loading level. The orthogonal tunability of these two parameters provides exceptional flexibility for SAC design, further underscoring the novelty and practicality of our method.

To investigate the relationship between sintering temperature and the structure of SACs, the structural characteristics of the catalysts prepared at different pyrolysis temperatures (450,550,650°C) were characterized. TGA analysis reveals that the pyrolysis process of Fe-SAC precursor can be divided into three stages (Supplementary Fig. 5): decomposition of thermally unstable oxalate component (80–250°C), polycondensation of melamine to form the catalyst substrate (250–350°C), and stabilization of atomic sites via metal capture of N-coordination species (350–550°C).

As shown in Supplementary Fig. 8a, XRD analysis proved that no diffraction peaks of the metal phase were observed for the catalyst prepared at 450℃, and no metal particle aggregates were observed by HRTEM (Supplementary Fig. 8b), indicating the formation of Fe-SACs during calcination at 450℃. However, the incomplete decomposition of unstable components in the substrate resulted in a relatively low metal proportion, with a loading of 15.3 wt% (Supplementary Table 1). In contrast, calcination at 550℃ produced Fe-SACs with a high metal loading of 41.31 wt%. Further increasing the temperature to 650℃ led to the emergence of distinct lattice diffraction peaks in the XRD patterns (Supplementary Fig. 8a), indicating intensified thermal motion of metal atoms at elevated temperatures and subsequent formation of crystalline structures (Supplementary Fig. 8d). Therefore, 550℃ is identified as the optimal synthesis temperature for preparing high-loading single-atom catalysts.

Comment 2. The manuscript suggests that oxalate plays a critical role in forming a supramolecular network with metal ions and melamine during the precursor stage, thereby enhancing SAC loading. However, the authors do not quantitatively investigate the relationship between the amount of oxalate added and the final SAC loading. Furthermore, there is no in-depth discussion on how oxalate contributes to the high metal loading or how its addition influences the synthesis process. This lack of quantitative analysis and mechanistic insight is a significant drawback, particularly for scaling up the synthesis process, as it leaves key parameters undefined.

Response:

We sincerely appreciate the reviewer's insightful comments on the role of oxalate in our synthesis strategy. The relationship between oxalate dosage and SAC loading is indeed critical for both mechanistic understanding and scalable production. Below, we provide a comprehensive clarification supported by quantitative experimental evidence and mechanism analysis.

As elaborated in Comment 1, OA has dual functions: (1) coordinating and chelating metal ions, and (2) chemically assembling with melamine. In the design of this study, the primary role of oxalate is to act as a specific carrier that anchors and delivers metal ions into the synchronously formed supramolecular organic framework, rather than directly modulating the metal loading. Comparatively, we adopted a more straightforward approach of controlling the concentration of iron salts **while keeping OA and MA constant** to precisely regulate the metal loading (**Supplementary Table 1**), as this method ensures atomic-level dispersion while avoiding interference from OA-mediated framework mass variations.

Undoubtedly, quantitative investigation on the relationship between oxalate dosage and the final SAC loading provides new insights into regulating metal loading and deepens the understanding of catalyst synthesis mechanism. Following the reviewer's suggestion, we systematically varied the concentration of oxalic acid (OA) **while keeping metal salt and MA concentrations constant. Our findings reveal that OA dosage critically governs both the structural evolution of catalysts and SAC loading capacity.**

As shown in Supplementary Table 4, when the amount of OA added was 1.5 mmol, the MA-OA-Fe^{3+} supramolecular organic framework did not form. This is because the chelated Fe^{3+} ions fully occupy carboxyl groups in OA, thereby preventing the composite reactions between the carboxyls of OA and the amines of MA. This observation confirms the concentration-dependent interactions between MA, OA, and Fe^{3+}, where an optimal stoichiometric ratio is essential for supramolecular framework assembly (i.e., Fe-SAC precursor formation). When the OA dosage is ≥3.1 mmol, the supramolecular framework successfully self-assembled, and the precursor yield increases proportionally with the OA concentration. This indicates that at a fixed concentration of MA and Fe^{3+}, OA preferentially coordinates with Fe^{3+} before complexing with MA, and a higher OA content promotes framework growth.

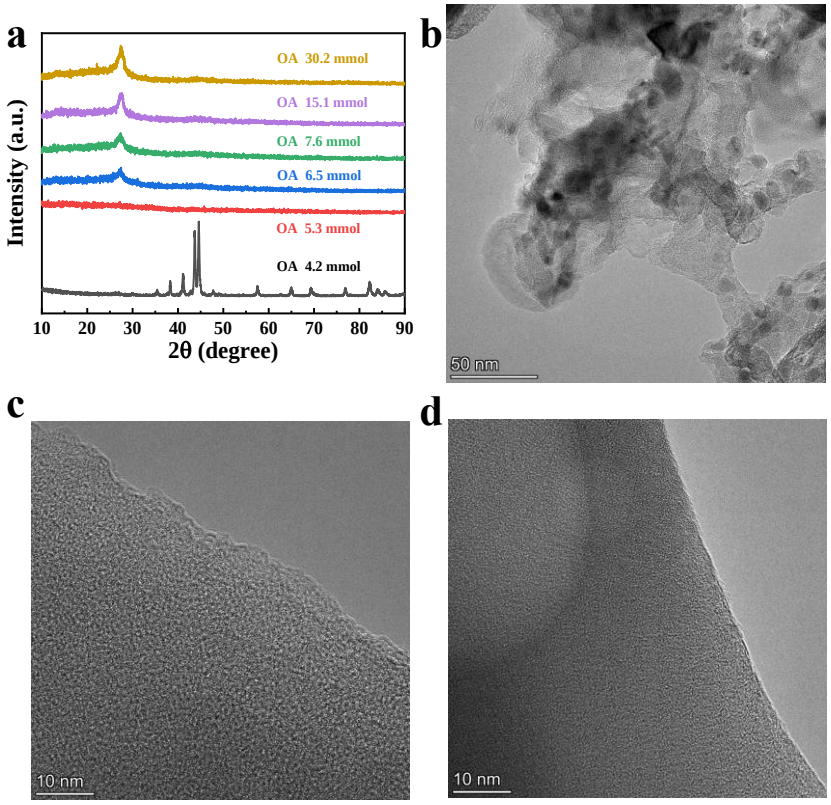

Supplementary Fig. 7 | a, XRD patterns of catalysts prepared with different OA amounts. b-d, HRTEM images of Fe-SAC at OA addition of 4.2, 5.3, and 30.2 mmol, respectively.

Supplementary Table 4 | Relationship between OA content, SAC precursor yield, and metal loading of as prepared SAC.

Number	OA (mmol)	SAC precursor yield (g)	SAC	Metal loads (wt%)
1	1.5	/	/	/
2	3.1	0.5305	No	/
3	4.2	0.8135	No	/
4	5.3	1.1324	Yes	39.8
5	6.5	1.4053	Yes	35.4
6	7.6	1.6483	Yes	31.2
7	15.1	2.0225	Yes	21.4
8	30.2	2.2318	Yes	17.2

Notably, at OA amount less than 4.2 mmol, the catalysts exhibited distinct XRD lattice diffraction peaks (Supplementary Fig. 6a), signifying Fe aggregation during pyrolysis. This phenomenon stems from the insufficient N-coordination species in the framework due to the limited formation of MA-OA composite at lower OA concentrations. Despite the generation of a small amount of supramolecular framework, the scarcity of N-coordination sites prevents the effective stabilization of anchored Fe atoms, leading to metal clustering.

In contrast, when the OA concentration was higher than 5.3 mmol, the resulting catalysts did not show XRD peaks of crystalline Fe phases (Supplementary Fig. 7a), and TEM confirmed the absence of metal aggregates (Supplementary Fig. 7). However, the Fe loading decreased with increasing OA amount. This inverse correlation is because higher OA dosage promotes the formation of MA-OA composite, thereby

increasing the total mass of carbon nitride substrate during pyrolysis. Consequently, the relative Fe mass loading decreases despite a constant absolute number of Fe atoms. These results demonstrate that rational regulation of OA concentration within an optimal range enables precise control of SAC metal loading while ensuring atomic dispersion.

We appreciate the reviewer's emphasis on the importance of quantitative mechanism analysis. Our systematic investigation reveals that oxalate acts as a "structure-directing agent" rather than just a sacrificial template. Its concentration governs framework integrity and metal stabilization capacity, while Fe^{3+} salt dosage directly controls the loading level. The orthogonal tunability of these two parameters provides exceptional flexibility for SAC design, further underscoring the novelty and practicality of our method.

Textual Revisions:

Lines 310-326:

Given the critical role of OA in coordinating metal ions, the amount of OA added was adjusted while maintaining a fixed concentration of MA and Fe salt. It was found that the OA content significantly influences the yield of the Fe-SAC precursor and the ultimate metal loading of the SAC (**Supplementary Table 4**). This demonstrates a concentration-dependent relationship between MA, OA, and Fe^{3+}, and reveals that the supramolecular organic framework possesses a maximum metal loading capacity. Increasing the OA content generates more catalyst substrate (**Supplementary Table 4**), resulting in a corresponding reduction in metal loading (Fig. 2e). This counterintuitive

phenomenon is the inverse of the trend observed in Fig. 2d, where increasing the Fe salt dosage while keeping MA and OA fixed gradually approaches the maximum loading capacity of framework, resulting in a rapid surge in metal loading. This systematic investigation reveals that oxalate acts as a "structure-directing agent" that governs framework integrity and metal stabilization capacity, rather than just a sacrificial template. The dosage of Fe^{3+} salt directly controls the loading level. The orthogonal tunability of these two parameters provides exceptional flexibility for SAC design, further underscoring the novelty and practicality of our method.

3. The decomposition of oxalate during calcination produces CO_2, which may disturb the condensation of melamine and affect the morphology, defects, and porosity of the C_3N_4 support. However, the authors do not systematically investigate whether varying the amount of oxalate can control the porosity and specific surface area of C_3N_4. Additionally, it remains unclear whether the micro- or mesopores generated by CO_2 release positively influence single-atom anchoring efficiency, reactant diffusion, or electron transfer. Excessive oxalate could also compromise the structural integrity of the C_3N_4 framework, potentially reducing catalyst stability or activity.

Response:

We sincerely appreciate the reviewer's insightful questions regarding the structural and functional implications of oxalate decomposition during synthesis. Below, we provide a systematic clarification supported by experimental evidence to address the role of CO_2 in modulating C_3N_4 porosity and the interplay between metal

loading and catalytic performance.

The primary objective of this study is to develop a facile method for synthesizing high-loading single-atom catalysts (SACs), thereby addressing the limitations of constrained metal loading and cumbersome synthesis protocols in existing approaches. Although the decomposition of oxalate during calcination does perturb the polycondensation of melamine (MA), the introduction of oxalic acid (OA) in our system does not detrimentally affect the morphology, defect structure, or porosity of the resulting C_3N_4 support. More critically, OA serves as a molecular bridge that (1) anchors metal ions through chelation and, (2) chemically links to MA molecules, ensuring atomic-level dispersion of metal species and full utilization of N-coordination sites within the substrate.

In our synthetic protocol, OA is not physically mixed with MA, but undergoes carboxyl-amino composite reactions to form a supramolecular organic framework. Prior to this assembly, OA molecules pre-chelate metal ions (e.g., Fe^{3+}), enabling targeted delivery of these ions into the framework. During the subsequent pyrolysis, the decomposition of OA releases CO_2, while the pre-anchored metal ions coordinate in situ with adjacent N atoms derived from MA. This molecular-level control ensures that the N-coordination species in the organic framework are fully exploited, thereby achieving ultrahigh metal loading without aggregation. This mechanism fundamentally differs from conventional physical mixing or post-impregnation methods, where N-coordination sites are randomly occupied and prone to underutilization.

To investigate whether oxalate influences the porosity and specific surface area of

C_3N_4, the morphology, surface area, and pore structure of C_3N_4 synthesized via direct pyrolysis of melamine (MA) and C_3N_4 prepared with MA+OA supramolecular framework were compared. The OA-free C_3N_4 exhibited a densely packed bulk structure (Supplementary Fig. 6), with a low specific surface area of 18.74 m^2 g^{-1}. In contrast, the introduction of OA resulted in a petal-like flaky architecture (Supplementary Fig. 6b), with a significantly enhanced specific surface area of 100.05 m^2 g^{-1}. This structural expansion is attributed to CO_2 liberated from the decomposed oxalate species during calcination, which disrupts the ordered polycondensation of melamine and generates hierarchical pores conducive to reactant diffusion in the catalytic processes.

Notably, the presence of metal components also impacts the porosity and surface area of the catalyst. As shown in Fig. 1h, at fixed concentrations of OA and MA, the specific surface area of the catalyst decreased with increasing metal loading. This trend arises because metal species catalyze the decomposition of unstable components and competitively scavenge nitrogen atoms from MA during pyrolysis, thereby hindering the polycondensation of the supramolecular polymer into ordered C_3N_4. This effect intensifies at higher metal loadings, as evidenced by the gradual disappearance of the characteristic heptazine unit diffraction peaks in the XRD patterns (Fig. 1g).

Importantly, although higher metal loading reduces surface area, electrochemical impedance spectroscopy (EIS) revealed a monotonic decrease in charge-transfer resistance (R_{ct}) with increasing metal content (Fig. 3d). This demonstrates that elevating the metal loading preferentially enhances electron transfer kinetics, compensating for

the diminished surface area. The superior electronic conductivity of high-loading Fe-SACs originates from the dense atomic Fe-N3C1 sites, which facilitate rapid electron tunneling in the carbon nitride matrix.

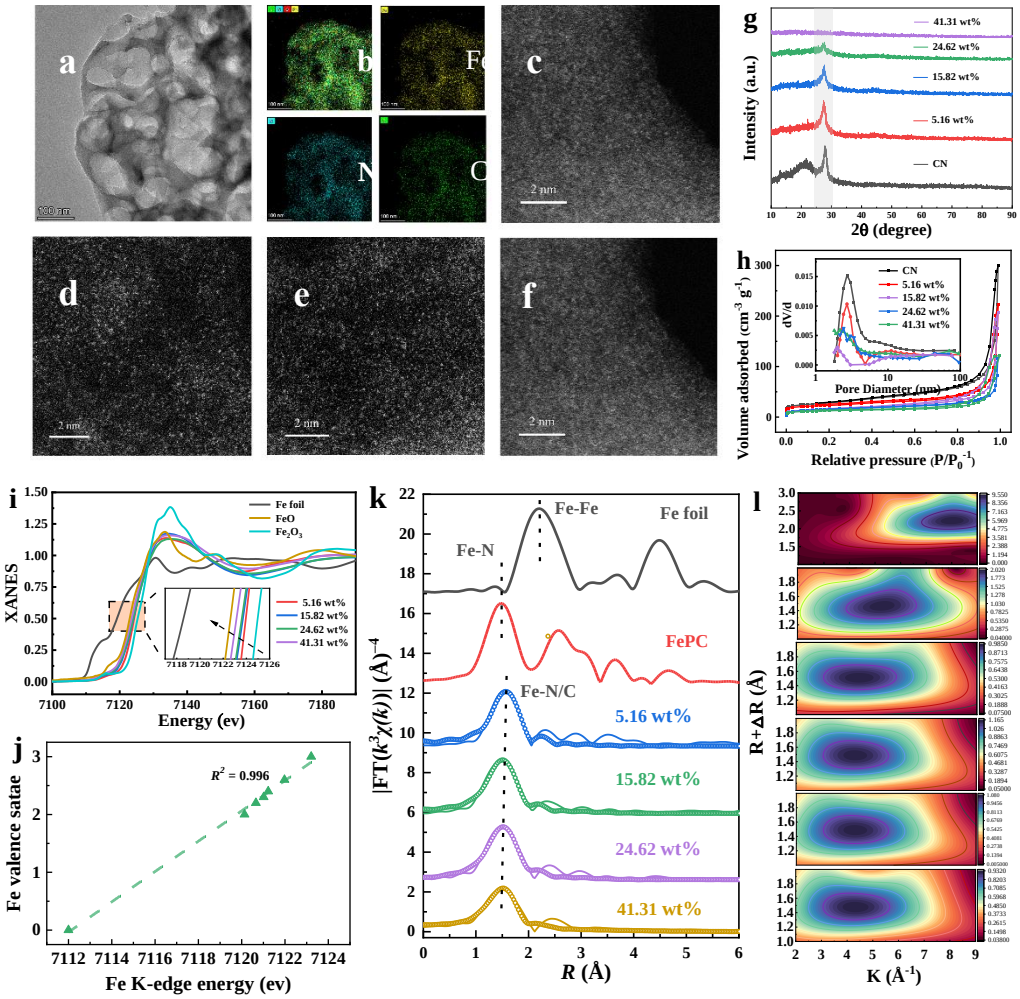

Fig. 1 | Structural characterizations of Fe-SAC-x. a-b, HRTEM and elemental mappings of Fe-SAC-41.31. c-f, HAADF-STEM images of Fe-SAC-x with metal loads was 41.31 wt%, 5.16 wt%, 15.82 wt% and 24.62 wt%, respectively. g, X-ray diffraction (XRD) patterns of as-prepared Fe-SAC-x. h, N_2 sorption isotherms and pore size distribution (inset) for iron-anchored catalysts with different iron loadings. i, Normalized XANES spectra of Fe-SAC-x samples. j, The oxidation state of iron decreased with the increase

of metal loading. k, k^3-weighted Fourier transforms. l, wavelet transform of the experimental EXAFS spectra of the indicated catalysts.

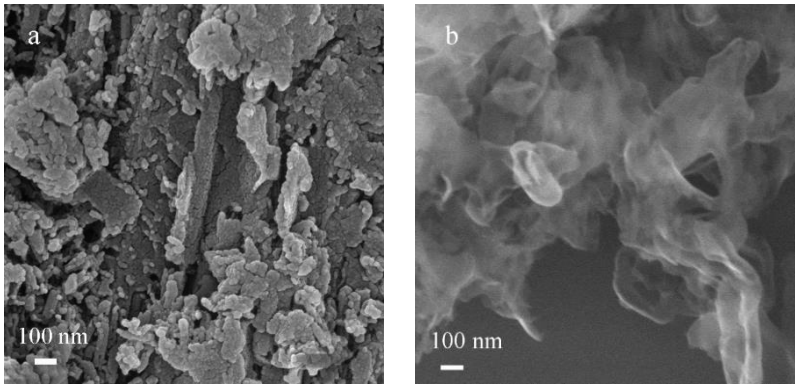

Supplementary Fig. 6 | SEM images of C_3N_4 prepared by pyrolysis of MA (a) or MA+OA supramolecular polymers (b).

Textual Revisions:

Lines 280-306:

The synthesis process of SAC through pyrolysis of supramolecular organic frameworks was monitored by thermogravimetric analysis (TGA) (Supplementary Fig. 5). The initial mass attenuation below 110℃ is attributed to the volatilization of residual moisture in the sample. A pronounced mass attenuation observed in the MA sample between 250-350℃ corresponds to its thermal polycondensation into C_3N_4. In contrast, the MA-OA composite supramolecular framework exhibited significant mass attenuation at lower temperatures due to the thermal decomposition of thermally labile oxalic acid. Notably, direct pyrolysis of MA without oxalic acid yielded C_3N_4 with a densely packed bulk structure (Supplementary Fig. 6a), demonstrating a specific

surface area of merely 18.74 m^2 g^{-1} (Supplementary Table 2). The pyrolysis of the supramolecular framework produced C_3N_4 with a petal-like flaky architecture (Supplementary Fig. 6b), exhibiting an enhanced specific surface area of 100.05 m^2 g^{-1}. This structural modification is ascribed to the liberation of CO_2 from the decomposed oxalate species during calcination, which disrupts the polycondensation of melamine and facilitates the formation of porous structures conducive to reactant diffusion in the catalytic processes. Remarkably, the Fe-SAC precursor anchored with Fe^{3+} ions displayed accelerated mass attenuation at reduced temperatures (Supplementary Fig. 5), indicating the catalytic role of Fe species in promoting the volatilization of thermally unstable components. Notably, the presence of metal components also impacts the porosity and surface area of the catalyst. As shown in Fig. 1h, at fixed concentrations of OA and MA, the specific surface area of the catalyst decreased with increasing metal loading. This trend arises because metal species catalyze the decomposition of unstable components and competitively scavenge nitrogen atoms from MA during pyrolysis, thereby hindering the polycondensation of the supramolecular polymer into ordered C_3N_4. This effect intensifies at higher metal loadings, as evidenced by the gradual disappearance of characteristic heptazine unit diffraction peaks in the XRD patterns (Fig. 1g).

4. Figure 2d reveals a non-linear, exponential relationship between the initial Fe^{3+} amount and the final iron content in the catalyst. The authors do not provide a satisfactory explanation for this phenomenon. For instance, they do not explore

whether there is a concentration-dependent coordination effect between oxalate and Fe^{3+} ions. A mechanistic explanation and experimental comparison are necessary to clarify why higher Fe salt concentrations lead to such an unusual increase in SAC loading. Without this, the synthesis process remains poorly understood.

Response:

We sincerely appreciate the reviewer's critical observation of the non-linear correlation between the initial Fe^{3+} dosage and final Fe loading. This relationship indeed reflects the inherent complex coordination equilibrium and framework saturation effect of our cascade anchoring strategy. Below, we provide a detailed mechanistic explanation supported by experimental evidence.

As elaborated in our response to Comment 2, the concentration-dependent interplay among melamine (MA), oxalic acid (OA), and Fe^{3+} governs the structural evolution, Fe dispersion, and ultimate loading of the catalyst. OA exhibits preferential chelation with Fe^{3+} ions over composite interactions with MA. Consequently, at fixed concentrations of OA and MA, increasing Fe^{3+} dosage enhances Fe^{3+}-OA complexation while suppressing OA-MA assembly. This is directly evidenced by the reduced yield of the supramolecular organic framework as the Fe^{3+} concentration rises (Supplementary Table 1).

Furthermore, the MA-OA supramolecular framework exhibits a finite Fe-loading capacity. As discussed in the response to Comment 2, at low OA concentrations, metal aggregation occurs because the Fe content exceeds the framework's loading threshold.

By increasing OA dosage, the yield of the supramolecular framework is enhanced, thereby elevating the framework's metal-loading capacity. This expansion can improve the Fe atomic dispersion while simultaneously reducing the Fe mass loading (the total substrate mass increases at fixed Fe quantities, leading to a proportional decrease in Fe mass fraction).

Analogously, when MA and OA concentrations are fixed, increasing Fe^{3+} dosage gradually approaches the saturation limit of the framework. Beyond this threshold, unchelated Fe^{3+} ions cannot be stably anchored within the framework, resulting in a nonlinear, exponential relationship between the initial Fe^{3+} concentration and the final Fe content in the catalyst. This saturation behavior mirrors Langmuir-type adsorption dynamics, where the availability of finite coordination sites governs the loading efficiency.

Textual Revisions:

Lines 307-327:

Intriguingly, for the final synthesized SAC, its Fe mass fraction increases nonlinearly with iron salt content in precursors (Fig. 2d). This indicates that a smaller incremental increase in Fe salt injection in the later stage can cause a significant rise in Fe loading. To elucidate this anomalous behavior, we systematically investigated the synthesis process of high-loading Fe-SACs. Given the critical role of OA in coordinating metal ions, the amount of OA added was adjusted while maintaining a fixed concentration of MA and Fe salt. It was found that the OA content significantly influences the yield of Fe-SAC precursor and the ultimate metal loading of SAC

(Supplementary Table 4). This demonstrates a concentration-dependent relationship between MA, OA, and Fe^{3+}, and reveals that the supramolecular organic framework possesses a maximum metal loading capacity. Increasing the OA content generates more catalyst substrate (Supplementary Table 4), resulting in a corresponding reduction in metal loading (Fig. 2e). This counterintuitive phenomenon is the inverse of the trend observed in Fig. 2d, where increasing the Fe salt dosage while keeping MA and OA fixed gradually approaches the maximum loading capacity of the framework, resulting in a rapid surge in metal loading. This systematic investigation reveals that oxalate acts as a "structure-directing agent" that governs framework integrity and metal stabilization capacity, rather than just a sacrificial template. The dosage of Fe^{3+} salt directly controls the loading level. The orthogonal tunability of these two parameters provides exceptional flexibility for SAC design, further underscoring the novelty and practicality of our method.

5. The manuscript lacks a thorough discussion on the coordination environment of single iron atoms at different loadings. Although Figure 2k shows no Fe-Fe coordination peak in the second coordination shell, suggesting the absence of short-range metal-metal bonding, at such high iron loadings (e.g., 41 wt%), there may be more distant or indirect Fe-Fe interactions. These interactions could slightly alter the bond length or coordination environment of the single Fe atoms, potentially influencing catalytic performance.

Response:

Thank you for raising this critical point regarding potential long-range interactions between high-density Fe single-atom sites, even in the absence of short-range Fe-Fe bonding. We thoroughly agree that ultrahigh metal loading (e.g., 41 wt%) may introduce subtle yet consequential electronic coupling effects, and we appreciate the opportunity to clarify these findings.

To systematically address this, we have performed DFT+U calculations (U = 3.29 eV for Fe 3d orbitals [7, 8]) to probe the coordination environment and electronic coupling of Fe sites at varying loadings. The key findings include:

Textual Revisions:

Lines 396-417:

Notably, the evolution of coordination environment occurred with the increase of metal loading. Specifically, the Fe-N/C bond lengths increase from 2.08 Å (5.16 wt%) to 2.13 Å (41.31 wt%) (Supplementary Table 6), reflecting the weakening of local hybridization. Meanwhile, PDOS analysis shows diminished overlap between Fe 3d and C/N 2p states at higher loadings (Supplementary Fig. 17). This reduction in orbital overlap corroborates the structural relaxation observed in bond lengths. It is worth noting that long-range electronic coupling was observed through the d-band shift. The Fe d-band center shifts negatively from −1.51 eV to −2.72 eV relative to the Fermi level as the loading increases, indicating enhanced metal-support charge transfer [6], which is consistent with the analysis results of bader charge (Supplementary Table 6) and charge density difference (Supplementary Fig. 18). These findings demonstrate that an increase in single-atom loading optimizes the proximity between adjacent Fe sites,

inducing long-range Fe-Fe interactions mediated by the support. Such long-range interactions modulate the electronic structure of Fe atoms and the hybridization of atomic orbitals with coordinated atoms, thereby optimizing the adsorption/desorption kinetics of reactive intermediates. Specifically, the downshifted d-band weakens the intermediate binding strength, while the enhanced electron transfer kinetics through long-range coupling may improve catalytic efficiency, as evidenced by the reduced R_{ct} in EIS below (Fig. 3d). Consequently, tailoring metal site density enables precise electronic structure modulation and facilitates efficient electron transfer through improved hybridization and bonding interactions between metal atomic orbitals, ultimately influencing catalytic performance.

Supplementary Table 6 | Fe coordination bond lengths and bader charges under different loadings.

Sample	Fe-C (Å)	Fe-N (Å)	Bader (Fe)
Fe-SAC 5.16 wt%	1.623	2.024	7.135
Fe-SAC 15.82 wt%	1.632	2.033	7.151
Fe-SAC 24.62 wt%	1.640	2.054	7.160
Fe-SAC 41.31 wt%	1.657	2.087	7.162

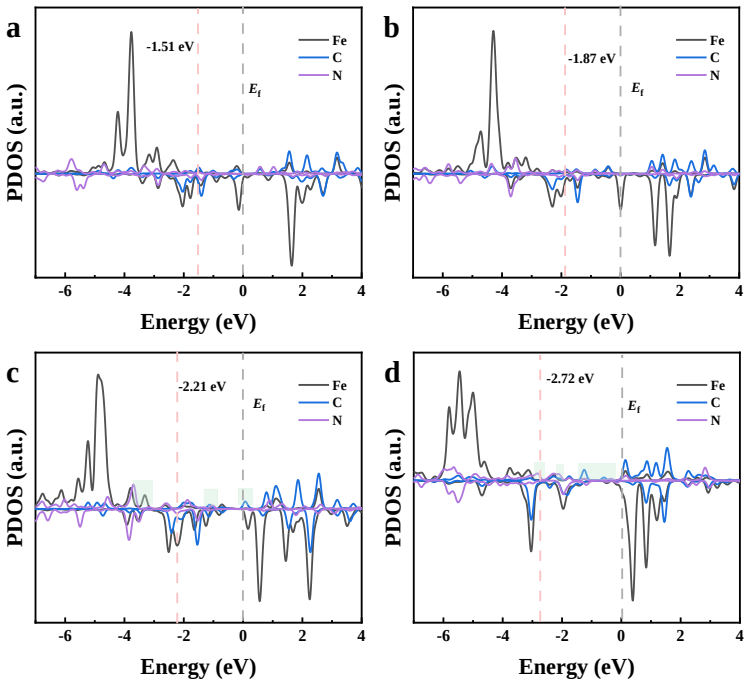

Supplementary Fig. 16 | Projected density of state (PDOS) of Fe 3d, N 2p, and C 2p orbital of Fe-SAC-5.16 (a), Fe-SAC-15.82 (b), Fe-SAC-24.62 (c) and Fe-SAC-41.31 (d), respectively.

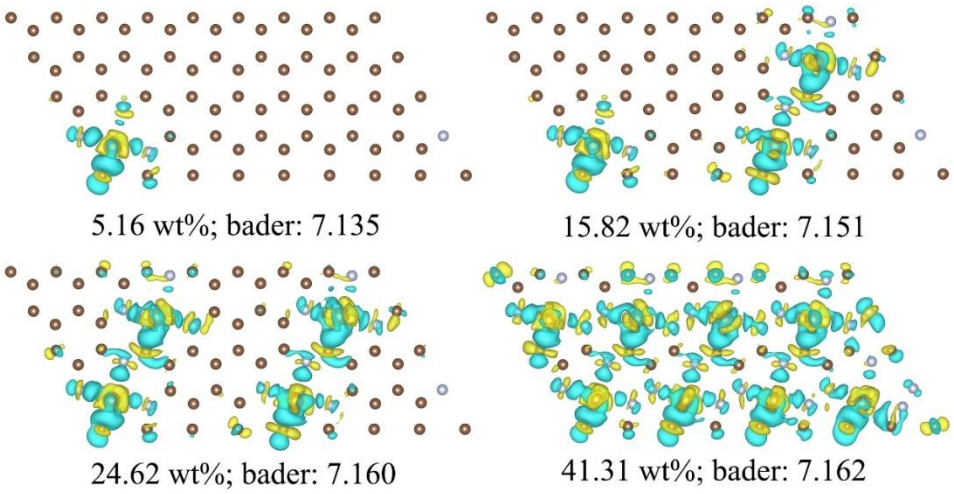

Supplementary Fig. 17 | Differential charge density of Fe–SAC-x models.

6. From a kinetic perspective, the apparent rate constant k should theoretically exhibit a linear or quasi-linear relationship with the total number of

active sites, assuming each site has similar intrinsic activity. However, the authors do not thoroughly discuss the specific relationship between k and the number of active sites in Figures 3a and S16. If the relationship is nonlinear, and catalytic kinetics accelerate significantly at high loadings, this could suggest the presence of long-distance Fe-Fe interactions that enhance catalytic activity. This point requires further analysis to clarify the underlying mechanisms driving the observed kinetics.

7. The authors propose that high iron loading not only provides more active centers but also thermodynamically facilitates PMS activation, leading to superior pollutant degradation performance. They hypothesize that this is related to Fe-Fe remote interactions. However, the manuscript does not investigate whether there is a critical loading at which these remote interactions become significantly enhanced, thereby playing a crucial role in lowering energy barriers or improving electron transfer efficiency. This is a key aspect that requires further experimental validation to support the proposed hypothesis.

Response to Comments 6 & 7:

We sincerely appreciate the reviewer's insightful observations on the nonlinear relationship between catalytic activity and metal loading, as well as the potential role of long-range Fe-Fe interactions. Your comments have guided us to perform deeper analysis to elucidate the mechanistic origins of the enhanced kinetics at high loadings. Below, we present a consolidated response supported by experimental and computational evidence. Due to the strong relevance between Comment 6 and 7, we

have consolidated our response to address these issues collectively:

In accordance with the reviewer's suggestions, we performed fitting of the relationship between metal loading and the apparent rate constant (k), and Fig. 4f revealed a positive correlation between k and the number of active sites. Assuming that each site exhibits similar intrinsic activity, the apparent rate constant k should theoretically display a linear or quasi-linear relationship with the total number of active sites. However, as noted by the reviewer, this positive correlation is non-linear in Fig. 4f, and the catalytic kinetics are significantly accelerated at high loadings. This non-linear, exponential positive correlation, combined with electronic structure changes of Fe sites at high loadings, collectively demonstrates the potential existence of long-range Fe-Fe interactions at elevated metal loadings, which enhances the catalytic activity of active sites. Notably, when the metal loading exceeds 24.62 wt%, the evolution of k values accelerates markedly, suggesting the existence of a critical loading threshold beyond which these long-range interactions become significantly enhanced.

To validate the above conclusions, we investigated the PMS catalytic performance at identical Fe active sites in catalyst models with varying metal loadings by DFT. It was observed that the PMS adsorption energy significantly increased when the metal loading reached 24.62 wt%, and as the loading continued to rise, the adsorption energy further changed (Fig. 4g). Additionally, the interaction between Fe sites and PMS exhibited enhanced differentiation due to intermetallic effects. Specifically, the electron depletion region of the Fe adsorption center expanded markedly, while the bonded O atom accumulated more electrons. Bader charge analysis further revealed an increase

in electron transfer from isolated Fe atoms to PMS molecules under higher Fe loading (Fig. 4g). This demonstrates that long-range metallic interactions at high loadings facilitate the activation of PMS by Fe site. This result is consistent with the open circuit potential test, indicating that catalysts with higher mass loading triggered higher potential jumps (Fig.4a). Catalysts with higher metal loading simultaneously exhibited lower charge transfer resistance (Fig. 3d), which collectively proves that elevated metal loading is beneficial for promoting the conductive bridging of Fe atoms to facilitate charge migration. Notably, when the metal loading surpassed the critical threshold of 24.62 wt%, the energy barriers of the $^1O_2$ generation pathway and rate-determining step (RDS) decreased substantially (Fig. 4h, $\Delta E_{rds,41.31} = 1.16$ eV $<$ $\Delta E_{rds,24.62} = 1.19$ eV $<$ $\Delta E_{rds,15.82} = 1.47$ eV $<$ $\Delta E_{rds,5.16} = 2.12$ eV). These theoretical analyses, combined with experimental results, including OCP (Fig. 4a), i-t curves (Fig. 4b), and SMX degradation kinetics (Fig. 4f), collectively demonstrate that long-range Fe-Fe interactions are significantly enhanced beyond the critical loading threshold of 24.62 wt%. These interactions play a pivotal role in reducing energy barriers and improving electron transfer efficiency.

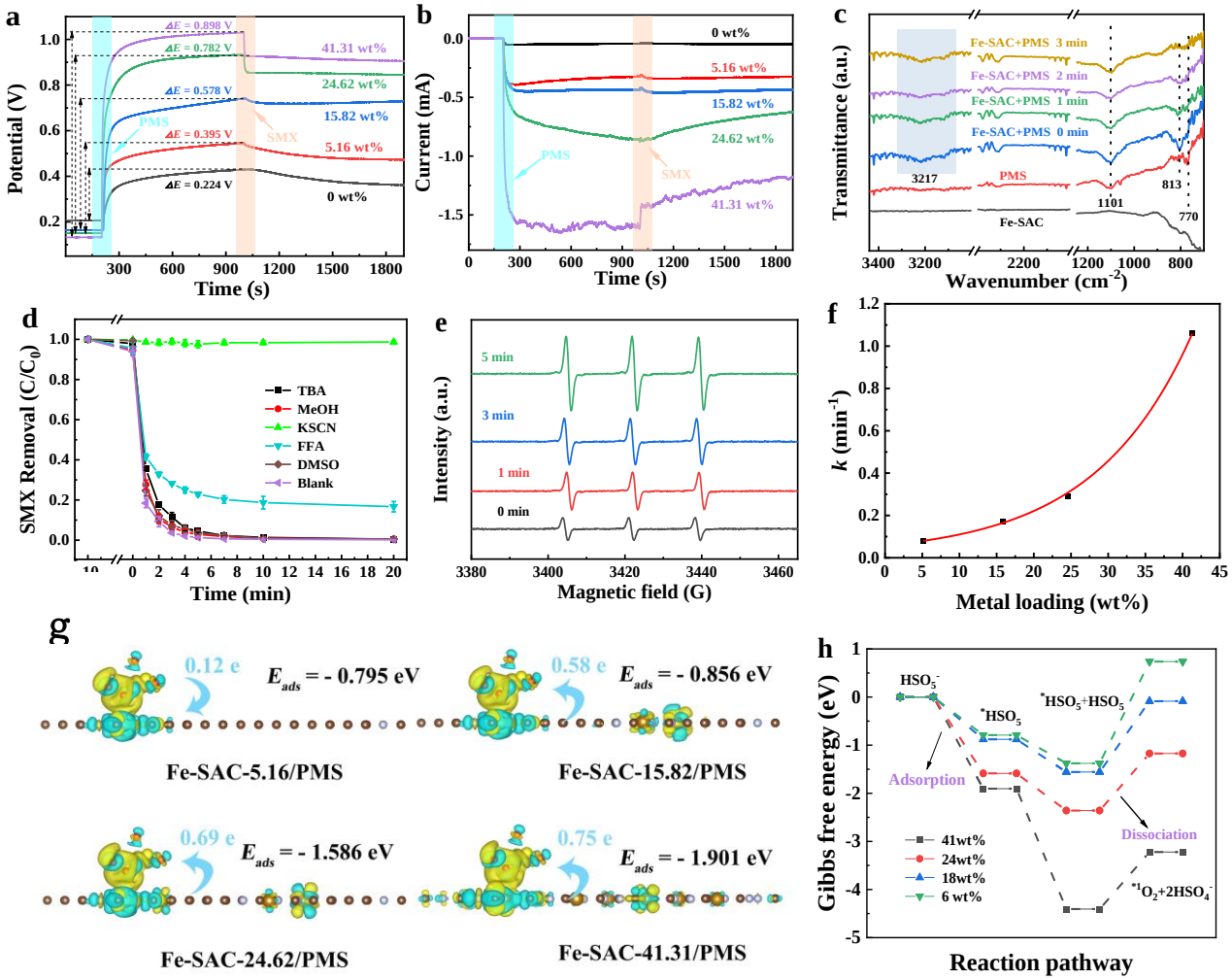

Fig. 4 | Evaluation of catalytic mechanism under gradient metal loading. a, The open-circuit potential changes of Fe-SAC-x when PMS or SMX is added respectively. b, Effects of PMS or SMX addition on the i-t curves at the corresponding open circuit potential. c, In situ FTIR spectra of Fe-SAC, PMS alone, and Fe-SAC combined with PMS. d, Effects of quenching reactive oxygen species on the degradation of SMX. e, Electron paramagnetic resonance spectra of TEMP-$^1O_2$ during SMX degradation in the Fe-SAC-4.31/PMS system. f, The relationship between metal loading and the apparent rate constant (k). g, Adsorption energy of PMS by Fe-SAC-x and the differential charge

density, bader charge transfer after the adsorption of PMS by Fe-SAC-x with different Fe loading. h, Energy profiles of $^1O_2$ derived reaction on varying Fe density models.

Textual Revisions:

Lines 673-707:

Notably, Fig. 4f reveals a positive correlation between k and the number of active sites. However, this positive correlation is non-linear, and the catalytic kinetics are significantly accelerated at high loadings. Assuming that each site exhibits similar intrinsic activity, the apparent rate constant k should theoretically display a linear or quasi-linear relationship with the total number of active sites. Combined with the electronic structure changes of Fe sites at high loadings, it collectively demonstrates the potential existence of long-range Fe-Fe interactions at elevated metal loadings, which enhances the catalytic activity of active sites. In addition, when the metal loading exceeds 24.62 wt%, the evolution of k values accelerates markedly, suggesting the existence of a critical loading threshold beyond which these long-range interactions become significantly enhanced.

To validate the above conclusions, we investigated the PMS catalytic performance at identical Fe active sites in catalyst models with varying metal loadings by DFT. It was observed that the PMS adsorption energy significantly increased when the metal loading reached 24.62 wt%, and as the loading continued to rise, the adsorption energy further changed (Fig. 4g). Additionally, the interaction between Fe sites and PMS exhibited enhanced differentiation due to intermetallic effects. Specifically, the electron

depletion region of the Fe adsorption center expanded markedly, while the bonded O atom accumulated more electrons. Bader charge analysis further revealed an increase in electron transfer from isolated Fe atoms to PMS molecules under higher Fe loading (Fig. 4g). This demonstrates that long-range metallic interactions at high loadings facilitate the activation of PMS by Fe site. This result is consistent with the open circuit potential test, indicating that catalysts with higher mass loading triggered higher potential jumps (Fig.4a). Catalysts with higher metal loading simultaneously exhibited lower charge transfer resistance (Fig. 3d), which collectively proves that elevated metal loading is beneficial for promoting the conductive bridging of Fe atoms to facilitate charge migration. Notably, when the metal loading surpassed the critical threshold of 24.62 wt%, the energy barriers of the $^1O_2$ generation pathway and rate-determining step (RDS) decreased substantially (Fig. 4h, $\Delta E_{rds,41.31} = 1.16$ eV $<$ $\Delta E_{rds,24.62} = 1.19$ eV $<$ $\Delta E_{rds,15.82} = 1.47$ eV $<$ $\Delta E_{rds,5.16} = 2.12$ eV). These theoretical analyses, combined with experimental results, including OCP (Fig. 4a), i-t curves (Fig. 4b), and SMX degradation kinetics (Fig. 4f), collectively demonstrate that long-range Fe-Fe interactions are significantly enhanced beyond the critical loading threshold of 24.62 wt%. These interactions play a pivotal role in reducing energy barriers and improving electron transfer efficiency.

8. Figures 2g-i demonstrate that other metals (Mn, Ag, La) can also be dispersed at high loadings. However, the authors do not discuss whether the choice of metal salt (e.g., chlorides) affects the cascade anchoring process. This omission

limits the understanding of the method's generalizability and applicability to other metal systems. A more comprehensive discussion on the influence of different metal precursors is necessary to establish the broader utility of the proposed synthesis strategy.

Response:

We sincerely appreciate the reviewer's insightful observation on the potential influence of metal salt precursors on the cascade anchoring process. To address this critical point, we conducted systematic experiments by substituting $Fe(NO_3)_3 \cdot 9H_2O$ with equimolar $Fe_2(SO_4)_3$ and $FeCl_3 \cdot 6H_2O$ while keeping all other synthesis parameters unchanged.

XRD (Supplementary Fig. 21) and HAADF-STEM (Supplementary Fig. 22) characterizations confirm the absence of crystalline phases and the atomic dispersion of Fe. ICP analysis reveals that Fe-SACs synthesized using $Fe_2(SO_4)_3$ and $FeCl_3 \cdot 6H_2O$ achieve metal loadings of 37 wt% and 40.04 wt%, respectively (Fig. 2f). These results demonstrate that anions such as SO_4^{2-}, Cl^-, and NO_3^- do not interfere with the cascade anchoring process, further validating the universal applicability of this method.

Textual Revisions:

Lines 431-436:

In addition, the choice of metal salt (e.g., chlorides or sulfate) do not interfere with the cascade anchoring process. XRD (Supplementary Fig. 21) and HAADF-STEM (Supplementary Fig. 22) characterizations confirm the absence of crystalline phases and the atomic dispersion of Fe. ICP analysis reveals that Fe-SACs synthesized using

$Fe_2(SO_4)_3$ and $FeCl_3 \cdot 6H_2O$ achieve metal loadings of 37 wt% and 40.04 wt%, respectively (Fig. 2f), further validating the universal applicability of this method.

9. The manuscript does not provide a detailed discussion on the relationship between sintering temperature and the structure of SACs. Sintering temperatureTG is a critical parameter that can significantly influence the stability, dispersion, and activity of single-atom sites. A more in-depth exploration of this aspect is essential to optimize the synthesis process and ensure the reproducibility of the high-loading SACs.

Response:

We sincerely appreciate the reviewer's critical observation regarding the pivotal role of sintering temperature in determining the stability, dispersion, and activity of single-atom catalysts (SACs). To address this issue, we systematically investigated the relationship between calcination temperature and SAC structure by synthesizing Fe-SACs at 450℃, 550℃, and 650℃, followed by comprehensive structural characterization.

Textual Revisions:

Lines 327-348:

To investigate the relationship between sintering temperature and the structure of SACs, the structural characteristics of the catalysts prepared at different pyrolysis temperatures (450, 550, 650℃) were characterized. TGA analysis reveals that the pyrolysis process of Fe-SAC precursor can be divided into three stages (Supplementary

Fig. 5): decomposition of thermally unstable oxalate component (80–250℃), polycondensation of melamine to form the catalyst substrate (250–350℃), and stabilization of atomic sites via metal capture of N-coordination species (350–550℃). As shown in Supplementary Fig. 8a, XRD analysis proved that no diffraction peaks of the metal phase were observed for the catalyst prepared at 450℃, and no metal particle aggregates were observed by HRTEM (Supplementary Fig. 8b), indicating the formation of Fe-SACs during calcination at 450℃. However, the incomplete decomposition of unstable components in the substrate resulted in a relatively low metal proportion, with a loading of 15.3 wt% (Supplementary Table 1). In contrast, calcination at 550℃ produced Fe-SACs with a high metal loading of 41.31 wt%. Further increasing the temperature to 650℃ led to the emergence of distinct lattice diffraction peaks in the XRD patterns (Supplementary Fig. 8a), indicating intensified thermal motion of metal atoms at elevated temperatures and subsequent formation of crystalline structures (Supplementary Fig. 8d). Therefore, 550℃ is identified as the optimal synthesis temperature for preparing high-loading single-atom catalysts.

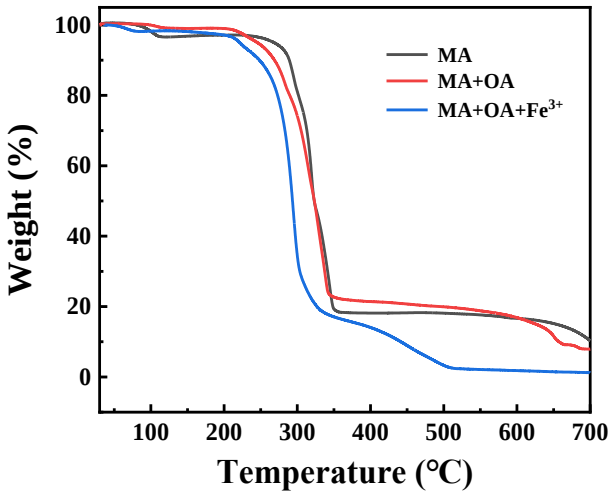

Supplementary Fig. 5 | Thermogravimetric curves of MA, MA+OA supramolecular organic skeleton and Fe-SAC precursor, respectively.

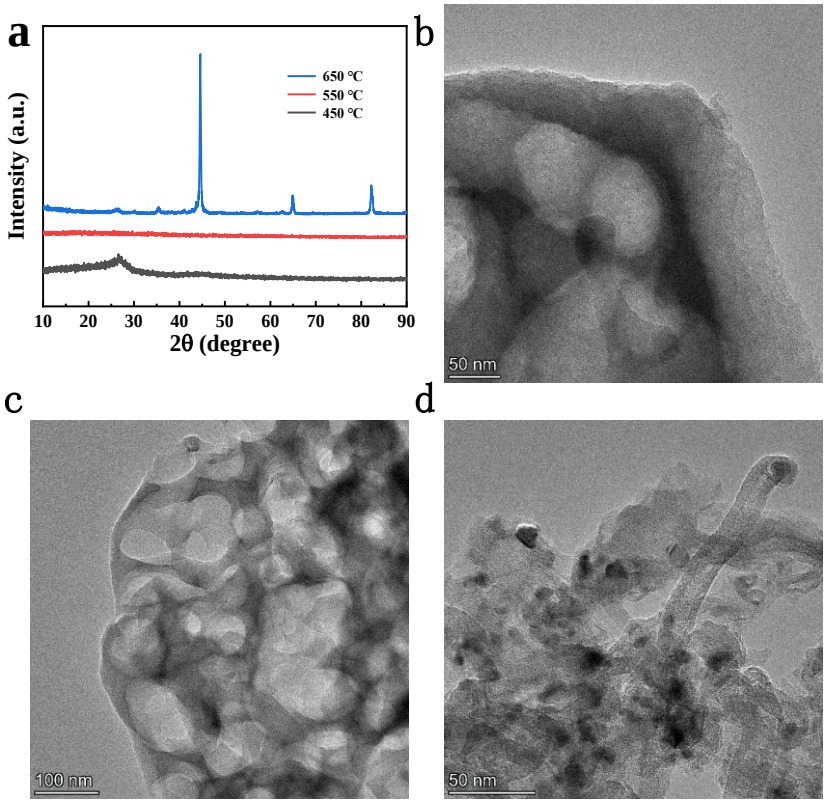

Supplementary Fig. 8 | a, XRD patterns of catalysts calcined at different temperature. b-d, HRTEM images of catalysts calcined at 450, 550 and 650°C, respectively.

Reviewer #4:

I co-reviewed this manuscript with one of the reviewers who provided the listed reports. This is part of the Nature Communications initiative to facilitate training in peer review and to provide appropriate recognition for Early Career Researchers who co-review manuscripts.

Response:

We deeply appreciate your rigorous evaluation and profound insights that have fundamentally improved the scientific rigor of this work. Your pivotal comments have guided us to make systematic revisions involving substantial experimental and theoretical enhancements.

We are grateful for the opportunity to establish a more rigorous research paradigm for ultrahigh-density SACs through the reviewer's expert guidance, which significantly advances the methodological standard in this field. We have addressed all comments point-by-point in the revised manuscript. Thank you again for your time and dedication in improving this research.

References

1. Han L*, et al.* A single-atom library for guided monometallic and concentration-complex multimetallic designs. *Nat Mater* **21**, 681-688 (2022).
2. Xiaowei L, Jean-Charles R, Suyuan Y. Effect of temperature on graphite oxidation behavior. *Nuclear Engineering and Design* **227**, 273-280 (2004).
3. Li D, Li H, Wen Q, Gao C, Song F, Zhou J. Investigation on Photo-Assisted Fenton-like Mechanism of Single-Atom Mn–N–Fe–N–Ni Charge Transfer Bridge Across Six-Membered Cavity of Graphitic Carbon Nitride. *Adv. Funct. Mater.* **34**, 2313631 (2024).
4. Li T*, et al.* Electron Filling Control Mechanism Triggered by the Penetration Effect in Fe3N/Fe Accelerates Sulfur Redox Kinetics. *Advanced Functional Materials* **n/a**, 2505615.
5. Shen J*, et al.* Atomic Engineering of Single-Atom Nanozymes for Biomedical Applications. *Adv. Mater.* **36**, (2024).
6. Ma PY*, et al.* Site-specific synergy in heterogeneous single atoms for efficient oxygen evolution. *Nat. Commun.* **16**, (2025).
7. He J, Ma SY, Zhou P, Zhang CX, He C, Sun LZ. Magnetic Properties of Single Transition-Metal Atom Absorbed Graphdiyne and Graphyne Sheet from DFT+U Calculations. *The Journal of Physical Chemistry C* **116**, 26313-26321 (2012).
8. Xu H, Cheng D, Cao D, Zeng XC. Revisiting the universal principle for the rational design of single-atom electrocatalysts. *Nat. Catal.* **7**, 207-218 (2024).
9. Li S*, et al.* Performance enhancement and mechanism of electroenhanced peroxymonosulfate activation by single-atom Fe catalyst modified electrodes. *Proc Natl Acad Sci USA* **121**, e2404965121 (2024).

10. Hai X*, et al.* Scalable two-step annealing method for preparing ultra-high-density single-atom catalyst libraries. *Nat. Nano.* **17**, 174-181 (2022).

11. Xiao X*, et al.* A promoted charge separation/transfer system from Cu single atoms and C_3N_4 layers for efficient photocatalysis. *Adv Mater* **32**, 2003082 (2020).

12. Su L, Wang P, Ma X, Wang J, Zhan S. Regulating local electron density of iron single sites by introducing nitrogen vacancies for efficient photo-fenton process. *Angew Chem Int Ed* **60**, 21261-21266 (2021).

13. Li JJ*, et al.* Highly active and stable metal single-atom catalysts achieved by strong electronic metal-support interactions. *J Am Chem Soc* **141**, 14515-14519 (2019).

14. Li F*, et al.* Revealing isolated $M{-}N_3C_1$ active sites for efficient collaborative oxygen reduction catalysis. *Angew Chem Int Ed* **59**, 23678-23683 (2020).

15. Hossain MD, Huang YF, Yu TH, Goddard WA, Luo ZT. Reaction mechanism and kinetics for CO_2 reduction on nickel single atom catalysts from quantum mechanics. *Nat Commun* **11**, 2256 (2020).

Facile cascade-anchored synthesis of ultrahigh metal loading single-atom for significantly improved Fenton-like catalysis

Shuaishuai Li[1,2,3], Wei Wang [1,2,3*], Huizhong Wu[1,2,3], Xuechun Wang[1,2,3], Shihu Ding[1,2,3], Jingyang Liu[1,2,3], Xiuwu Zhang[1,2,3], Jiangli Sun[1,2,3], Chunhong Fu[1,2,3], Minghua Zhou [1,2,3*]

[1] MOE Key Laboratory of Pollution Processes and Environmental Criteria, Tianjin Key Laboratory of Environmental Technology for Complex Trans-Media Pollution,

[2] Tianjin Advanced Water Treatment Technology International Joint Research Center, College of Environmental Science and Engineering, Nankai University, Tianjin 300350, China

[3] Carbon Neutrality Interdisciplinary Science Centre, College of Environmental Science and Engineering, Nankai University, Tianjin 300350, China

[*] Corresponding author. Tel/Fax: +86 022 23501117. E-mail address: zhoumh@nankai.edu.cn (M. Zhou), nkwangwei@126.com

Reviewer #1:

The authors have thoroughly addressed all of my concerns. They have provided detailed responses and made corresponding revisions to the manuscript. I am pleased to recommend the publication of this manuscript in Nature communications.

Response to Reviewer #1

We sincerely thank Reviewer #1 for their valuable insights and constructive feedback on our manuscript. We are delighted to hear that our revisions have adequately addressed all raised concerns. It is an honor to receive your positive assessment and recommendation for publication in *Nature Communications*. Your expertise has greatly strengthened our work, and we appreciate the time and effort dedicated to reviewing our research.

Reviewer #2:

I think this paper is acceptable now.

Response to Reviewer #2

We sincerely appreciate Reviewer #2's acknowledgment of our work and

confirmation that the manuscript now meets the standards for publication. Thank you for your time and rigorous evaluation throughout the review process.

Reviewer #3 and 4:

I co-reviewed this manuscript with one of the reviewers who provided the listed reports. This is part of the Nature Communications initiative to facilitate training in peer review and to provide appropriate recognition for Early Career Researchers who co-review manuscripts.

Response to Reviewer #3 and 4

We sincerely thank both reviewers for their rigorous yet constructive evaluation of our manuscript. We greatly appreciate Nature Communications' initiative to foster peer-review training for Early Career Researchers (ECRs).

The manuscript presents a strategy for synthesizing high-loading single-atom catalysts (SACs) and their application in activating peroxymonosulfate (PMS) for the degradation of organic pollutants. While the work demonstrates potential application value, several critical issues must be addressed before it can be considered for publication. Below are the detailed concerns that warrant rejection of the manuscript:

1. The proposed cascade anchoring method for synthesizing high-loading SACs lacks sufficient novelty. Similar approaches have been extensively reported in the literature (e.g., Adv. Mater. 2024, 36, 2404900; Nat. Chem. 2021, 13(9): 887-894; Nat. Commun. 2019, 10(1), 1278). Notably, the study in Nat. Commun. 2019 employed glucose as an anchor and C_3N_4 as the substrate, yet achieved significantly lower metal loading compared to the 41.31 wt% reported in this manuscript. The authors fail to provide a convincing explanation for the exceptionally high loading achieved in their work, nor do they elucidate the underlying mechanisms ensuring the stability of these high-loading SACs. Without a clear differentiation from existing methods and a robust mechanistic explanation, the novelty and scientific contribution of the synthesis strategy remain questionable.

2. The manuscript suggests that oxalate plays a critical role in forming a supramolecular network with metal ions and melamine during the precursor stage, thereby enhancing SAC loading. However, the authors do not quantitatively investigate the relationship between the amount of oxalate added and the final SAC loading. Furthermore, there is no in-depth discussion on how oxalate contributes to the high metal loading or how its addition influences the synthesis process. This lack of quantitative analysis and mechanistic insight is a significant drawback, particularly for scaling up the synthesis process, as it leaves key parameters undefined.

3. The decomposition of oxalate during calcination produces CO_2, which may disturb the condensation of melamine and affect the morphology, defects, and porosity of the C_3N_4 support. However, the authors do not systematically investigate whether varying the amount of oxalate can control the porosity and specific surface area of C_3N_4. Additionally, it remains unclear whether the micro- or mesopores generated by CO_2 release positively influence single-atom anchoring efficiency, reactant diffusion, or electron transfer. Excessive oxalate could also compromise the structural integrity of the C_3N_4 framework, potentially reducing catalyst

stability or activity.

4. Figure 2d reveals a non-linear, exponential relationship between the initial Fe^{3+} amount and the final iron content in the catalyst. The authors do not provide a satisfactory explanation for this phenomenon. For instance, they do not explore whether there is a concentration-dependent coordination effect between oxalate and Fe^{3+} ions. A mechanistic explanation and experimental comparison are necessary to clarify why higher Fe salt concentrations lead to such an unusual increase in SAC loading. Without this, the synthesis process remains poorly understood.

5. The manuscript lacks a thorough discussion on the coordination environment of single iron atoms at different loadings. Although Figure 2k shows no Fe-Fe coordination peak in the second coordination shell, suggesting the absence of short-range metal-metal bonding, at such high iron loadings (e.g., 41 wt%), there may be more distant or indirect Fe-Fe interactions. These interactions could slightly alter the bond length or coordination environment of the single Fe atoms, potentially influencing catalytic performance.

6. From a kinetic perspective, the apparent rate constant k should theoretically exhibit a linear or quasi-linear relationship with the total number of active sites, assuming each site has similar intrinsic activity. However, the authors do not thoroughly discuss the specific relationship between k and the number of active sites in Figures 3a and S16. If the relationship is nonlinear, and catalytic kinetics accelerate significantly at high loadings, this could suggest the presence of long-distance Fe-Fe interactions that enhance catalytic activity. This point requires further analysis to clarify the underlying mechanisms driving the observed kinetics.

7. The authors propose that high iron loading not only provides more active centers but also thermodynamically facilitates PMS activation, leading to superior pollutant degradation performance. They hypothesize that this is related to Fe-Fe remote interactions. However, the manuscript does not investigate whether there is a critical loading at which these remote interactions become significantly enhanced, thereby playing a crucial role in lowering energy barriers or improving electron transfer efficiency. This is a key aspect that requires further experimental validation to support the proposed hypothesis.

8. Figures 2g-i demonstrate that other metals (Mn, Ag, La) can also be dispersed at high loadings. However, the authors do not discuss whether the choice of metal salt (e.g., chlorides) affects the cascade anchoring process. This omission limits the understanding of the method's generalizability and applicability to other metal systems. A more comprehensive discussion on the influence of different metal precursors is necessary to establish the broader utility of the proposed synthesis strategy.

9. The manuscript does not provide a detailed discussion on the relationship between sintering temperature and the structure of the SACs. Sintering temperature is a critical parameter that can significantly influence the stability, dispersion, and activity of single-atom sites. A more in-depth exploration of this aspect is essential to optimize the synthesis process and ensure the reproducibility of the high-loading SACs.

In conclusion, while the manuscript presents an approach to synthesizing high-loading SACs, the lack of sufficient novelty, insufficient mechanistic insights, and unresolved critical issues lower its scientific rigor and potential impact. Addressing these concerns through additional experiments and a more thorough discussion would be necessary to strengthen the manuscript's contribution to the field. Until then, I recommend rejection of this work.